



1 **Lower-tropospheric CO<sub>2</sub> from near-infrared ACOS-GOSAT**  
2 **observations**

3  
4 Susan S. Kulawik<sup>1</sup>, Chris O'Dell<sup>2</sup>, Vivienne H. Payne<sup>3</sup>, Le Kuai<sup>4</sup>, Helen M.  
5 Worden<sup>5</sup>, Sebastien C. Biraud<sup>6</sup>, Colm Sweeney<sup>7</sup>, Britton Stephens<sup>7</sup>, Laura T.  
6 Iraci<sup>8</sup>, Emma L. Yates<sup>1</sup>, Tomoaki Tanaka<sup>8</sup>

7  
8 (1) Bay Area Environmental Research Institute, Sonoma, CA, USA

9 (2) Cooperative Institute for Research in the Atmosphere, Colorado State  
10 University, Fort Collins, CO, USA

11 (3) Jet Propulsion Laboratory, California Institute of Technology, Pasadena,  
12 CA, USA

13 (4) UCLA Joint Institute for Regional Earth System Science and Engineering  
14 (JIFRESSE), Los Angeles, CA, USA

15 (5) Atmospheric Chemistry Observations & Modeling (ACOM) Laboratory  
16 National Center for Atmospheric Research, Boulder CO 80307 USA

17 (6) Lawrence Berkeley National Laboratory, Earth Science Division, Berkeley,  
18 CA, USA

19 (7) NOAA/ESRL/GMD, Boulder, CO, USA

20 (8) NASA Ames, Moffett Field, CA, USA

21

22 **Abstract**

23 We present two new products from near-infrared GOSAT observations:  
24 lower tropospheric (LMT, from 0-2.5 km) and upper  
25 tropospheric/stratospheric (U, above 2.5 km) carbon dioxide partial columns.  
26 We compare these new products to aircraft profiles and remote surface flask  
27 measurements and find that the seasonal and year-to-year variations in the  
28 new partial columns significantly improve over the ACOS-GOSAT initial  
29 guess/a priori, with distinct patterns in the LMT and U seasonal cycles which  
30 match validation data. For land monthly averages, we find errors of 1.9,  
31 0.7, and 0.8 ppm for retrieved GOSAT LMT, U, and XCO<sub>2</sub>; for ocean monthly  
32 averages, we find errors of 0.7, 0.5, and 0.5 ppm for retrieved GOSAT LMT,  
33 U, and XCO<sub>2</sub>. In the southern hemisphere biomass burning season, the new  
34 partial columns show similar patterns to MODIS fire maps and MOPITT  
35 multispectral CO for both vertical levels, despite a flat ACOS-GOSAT prior,  
36 and CO/CO<sub>2</sub> emission factor consistent with published values. The difference  
37 of LMT and U, useful for evaluation of model transport error, has also been  
38 validated with monthly average error of 0.8 (1.4) ppm for ocean (land). The  
39 new LMT partial column is more locally influenced than the U partial column,  
40 meaning that local fluxes can now be separated from CO<sub>2</sub> transported from  
41 far away.

42

43 **1 Introduction**



44 The Greenhouse Gases Observing Satellite (GOSAT) has been measuring  
45 global satellite CO<sub>2</sub> columns since 2009, achieving accuracy to 0.3 ppm in  
46 regional biases and 1.7 ppm single observation error (Kulawik et al., 2016).  
47 The sensitivity of near-infrared radiances to CO<sub>2</sub> varies by altitude differently  
48 in the strong and weak bands, resulting in the capability of retrieving  
49 multiple pieces of vertical information from near-infrared observations, with  
50 3+ degrees of freedom (i.e. independent pieces of information) for TCCON  
51 (Connor et al., 2015; Kuai et al., 2012), 1.6 degrees of freedom for GOSAT  
52 (this paper), and 2.0 degrees of freedom for OCO-2 (Kulawik, unpublished  
53 result). In this paper we use the intermediate retrieved profile from ACOS-  
54 GOSAT processing to construct, bias-correct, and validate two partial  
55 columns from near-infrared GOSAT observations (schematically shown in  
56 Fig. 1). The partially correlated errors and sensitivity of these two partial  
57 columns are characterized so that they can be used for flux estimation and  
58 other science analyses.

59

60 An important goal of carbon cycle research is to improve top-down estimates  
61 of CO<sub>2</sub> fluxes, which use model assimilation to trace the observed variability  
62 in the long-lived tracer backwards to sources and sinks. Historically, such  
63 top-down flux estimates have relied on surface observations (e.g. Peters et  
64 al., 2007; Chevallier et al., 2010), though it was postulated 15 years ago  
65 that satellite-based measurements of column CO<sub>2</sub> could dramatically reduce  
66 top-down based flux uncertainties (Rayner and O'Brien, 2001; O'Brien and  
67 Rayner, 2002). Guided by this early work, most GOSAT analyses have  
68 focused solely on total column CO<sub>2</sub> (or XCO<sub>2</sub>). Separation of XCO<sub>2</sub> into two  
69 vertical columns has several advantages over column XCO<sub>2</sub> and surface  
70 observations which should improve our ability to accurately estimate fluxes:

71

- 72 • flux estimates from column measurements rely on observations up to  
73 continent-scales away (Liu et al., 2015; Feng et al., 2016); whereas  
74 LMT back-trajectories show a more local influence of surface fluxes  
75 versus for XCO<sub>2</sub>, making flux estimates more data driven by local  
76 measurements rather than relying on model transport, a major driver  
77 of flux uncertainties (Houweling et al., 2015; Liu et al., 2015;  
78 Chevallier et al., 2014; Liu et al., 2011; Prather et al., 2008)
- 79 • Stephens et al. (2007) show that measuring atmospheric values of  
80 carbon dioxide at 2 vertical levels better constrains model transport  
81 and partitioning between southern hemisphere land and northern mid-  
82 latitude land fluxes, since vertical transport is an uncertainty in flux  
83 estimates (Deng et al., 2015; Lauvaux and Davis, 2014; Stephens et  
84 al., 2007)
- 85 • The LMT covers at least the entire boundary layer which partially  
86 mitigates one source of flask assimilation error, the boundary layer



87 height (Denning et al., 1996; Gurney et al., 2002; Rayner and O'Brien,  
88 2001); and  
89 • GOSAT provides observations in many areas which are sparsely  
90 covered by surface-based measurements.

91

92 In this work, we evaluate the precision and accuracy of these new LMT and  
93 U partial column products derived from GOSAT, with the goal of providing  
94 more and better information to the flux inversion estimates than is available  
95 from the total column alone. This paper is structured as follows. We  
96 introduce the datasets used in Section 2, and the theoretical basis in Section  
97 3. Section 4 describes methodology, e.g. the coincidence criteria and  
98 GOSAT bias correction. Section 4.1 uses back-trajectories to estimate the  
99 distance to peak sensitivity to surface fluxes for LMT and U. Section 5 shows  
100 comparisons to aircraft observations and surface sites, including maps of the  
101 two partial columns. Section 5.4 shows patterns of the two partial columns  
102 versus MOPITT multi-spectral CO retrievals, and Section 5.5 looks at errors  
103 of LMT minus U. Section 6 discusses and summarizes these results.

104

## 105 **2. Datasets**

106 There are two datasets used for validation of the new partial columns.  
107 Aircraft profiles, which fly from the surface to somewhere between 5 and 13  
108 km, can be used to directly validate what is seen with the two GOSAT partial  
109 columns. The second dataset that is used is from remote surface flasks,  
110 which are used to compare to the lower GOSAT partial column, assuming  
111 that 0-2.5 km is well mixed at remote sites. TCCON, which currently  
112 measures full columns, is used to diagnose discrepancies between aircraft  
113 and GOSAT at the sites where both exist. Additionally, we compare signals  
114 from burning and transport in southern hemisphere land from GOSAT,  
115 MOPITT, and MODIS fire counts. Figure 2 shows aircraft and surface  
116 validation locations, along with GOSAT coincidences.

117

### 118 **2.1 GOSAT**

119 The Greenhouse gases Observing SATellite (GOSAT) takes measurements of  
120 reflected sunlight in three shortwave bands with a circular footprint of  
121 approximately 10.5 km diameter at nadir (Kuze et al., 2016; Yokota et al.,  
122 2009; Crisp et al., 2012). ACOS-GOSAT v3.5 from the lite product with  
123 quality flag of 0 are used along with the full profile, profile averaging kernel,  
124 and full profile error matrices from ancillary GOSAT files. We use both nadir  
125 land observations (looking straight down) and ocean glint observations  
126 (sunlint tracking mode), but not medium gain over land, as there is not  
127 sufficiently co-located validation data to validate medium gain observations.

128

### 129 **2.2 ESRL aircraft profiles**



130 Aircraft and ocean measurements are obtained from an obspack  
131 (co2\_1\_PROTOTYPE\_v1.0.4b\_2014-02-13). The measurements are  
132 extended down to the surface using the lowest measured value, and  
133 extended to the tropopause using the aircraft value at the highest altitude  
134 (The Tropopause is from NCEP,  
135 <http://www.esrl.noaa.gov/psd/data/gridded/data.ncep.reanalysis.html>). The  
136 CarbonTracker model (CT2015, see below) is used to extend the profile  
137 through the stratosphere.

138

### 139 **2.3 Remote oceanic surface in situ measurement sites**

140 Remote surface sites are from the Earth System Research Laboratory  
141 Observation Package (ObsPack) Data Product surface flask measurements  
142 (Conway et al., 1994), which are accurate to 0.1 ppm with excellent  
143 coverage in the US and Europe and sparser coverage elsewhere. For each  
144 station, there can be different options, represented by file names. The  
145 "afternoon" file is preferred, as it best matches the satellite overpass. If  
146 "afternoon" is not found, "nighttime" and "marine" (which filters  
147 observations by their source) are excluded, and "allvalid", "representative",  
148 and "continental" are accepted.

149

150 The "remote oceanic" locations used are selected to have at least 97% ocean  
151 at a 5 degree radius around the location. The locations are shown in Fig. 2.  
152 Although the air mass observed by GOSAT LMT will not match the air mass  
153 observed by the surface site, the remote location should result in boundary  
154 layer mixing that will make the comparisons useful. Additionally, these sites  
155 are not used in development of the bias correction terms (described in  
156 Section 3.5 and Appendix A) and are an independent test of bias correction  
157 for ocean.

158

### 159 **2.4 HIPPO aircraft profiles**

160 The HIAPER Pole-to-Pole Observations (HIPPO) project samples the  
161 atmosphere in a series of profiles from the surface to 9-13 km, from about  
162 80N to 60S. The campaigns covered different years as well as different  
163 seasons, namely: HIPPO 1: January, 2009, HIPPO 2: November 2009, HIPPO  
164 3: March-April, 2010, HIPPO 4: June-July, 2011, and HIPPO 5: August-  
165 September, 2011. Frankenberg et al. (2016) recently were successful in  
166 evaluating satellite measurements of column CO<sub>2</sub> over ocean (including  
167 GOSAT) using HIPPO. In this paper, we look at comparisons between GOSAT  
168 and HIPPO 2-5 (HIPPO 1 occurs prior to GOSAT launch) using the HIPPO-  
169 identified profiles and the CO<sub>2</sub>\_X field, based on 1s data averaged to 10s,  
170 from two (harmonized) sensors: CO<sub>2</sub>-QCLS and 15 CO<sub>2</sub>-OMS. Due to the  
171 GOSAT glint coverage span of about 40 degrees with additional screening for  
172 the new products, many of the comparisons had fairly limited latitudinal  
173 spans with the GOSAT improvement over the prior found more in improving



174 the bias rather than improving the standard deviation. The combined  
175 campaigns span a wide range of GOSAT latitudes.

176

### 177 **2.5 AJAX aircraft profiles**

178 The Alpha Jet Atmospheric eXperiment (AJAX) project collects in situ CO<sub>2</sub>  
179 vertical profiles from the surface to 8 km in several locations, including  
180 Railroad Valley, NV; Merced, CA, and other locations in the West Coast.  
181 Most of the version 4 profiles used in this paper were collected to coincide  
182 with GOSAT overpasses. Trace gas instruments and the Meteorological  
183 Measurement Sensor are housed in an unpressurized sensor pod that is  
184 mounted under the wing. A cavity ring-down spectrometer (Picarro Inc.  
185 G2301-m) which has been modified for flight conditions is routinely  
186 calibrated to NOAA/ESRL gas standards. Calculated 1 $\sigma$  overall uncertainties  
187 are 0.16 ppm for CO<sub>2</sub> (Hamill et al. 2016; Tanaka et al., 2016).

188

### 189 **2.6 MOPITT v6 multispectral CO retrieval**

190 In section 5, we utilize satellite-based CO observations from MOPITT to  
191 attribute spatial variability in LMT and U. The MOPITT instrument on EOS-  
192 Terra is in a sun-synchronous orbit with mean local time overpasses of  
193 10:30 and 22:30. It has global coverage in  $\sim$ 3 days with a 22km x 22km  
194 horizontal footprint. MOPITT uses gas filter correlation radiometry (GFCR) to  
195 measure atmospheric CO at 4.6  $\mu$ m (Thermal Infrared) and 2.3  $\mu$ m (Short-  
196 wave Infrared) and is the only satellite instrument capable of simultaneous  
197 multispectral retrievals of CO with enhanced sensitivity to near-surface CO  
198 for daytime/land observations (Worden et al., 2010). MOPITT CO data have  
199 been validated for each retrieval algorithm version using aircraft in situ  
200 measurements (Deeter et al., 2014). Here we use daytime only MOPITT V6J  
201 (multispectral) data that have been filtered to require cloud free scenes from  
202 both MOPITT and MODIS cloud detection. We also use a measure of  
203 sensitivity to near-surface CO computed from the trace of the averaging  
204 kernel for the bottom 2 pressure levels to select scenes that contain  
205 relatively more information from the measurement.

206

### 207 **2.7 MODIS fire counts**

208 MODIS fire counts (found at [https://lance.modaps.eosdis.nasa.gov/cgi-](https://lance.modaps.eosdis.nasa.gov/cgi-bin/imagery/firemaps.cgi)  
209 [bin/imagery/firemaps.cgi](https://lance.modaps.eosdis.nasa.gov/cgi-bin/imagery/firemaps.cgi)) are used to identify biomass burning locations.  
210 Fire maps are created by Jacques Descloitres with fire detection algorithm  
211 developed by Louis Giglio. Blue Marble background image created by Reto  
212 Stokli (Giglio et al., 2003; Davies et al., 2004).

213

### 214 **2.8 CarbonTracker model**

215 CarbonTracker CT2015, <http://carbontracker.noaa.gov>, (Peters et al., 2007)  
216 is used to extend aircraft profiles from the stratosphere to the top of the



217 atmosphere (similarly to in Frankenberg et al., 2016 and Inoue et al., 2013)  
218 and to quantify co-location error (similarly to Kulawik et al. (2016).

219

## 220 **2.9 TCCON**

221 The Total Carbon Column Observing Network (TCCON) observations, version  
222 GGG2014 (Wunch et al., 2011a) at Lamont (Wennberg et al., 2014) and  
223 Park Falls (Wennberg et al., 2014), where both aircraft and TCCON  
224 observations have co-located measurements, are used to evaluate XCO<sub>2</sub>  
225 calculated from the aircraft observations (extended as described by Section  
226 3.7). Although the TCCON observations contain information to split into 2 or  
227 3 vertical columns, the focus of the TCCON project has been on the  
228 validation of XCO<sub>2</sub> from OCO-2 and GOSAT. Recent work by Kuai et al.  
229 (2012), Dohe et al. (2012), and Connor et al. (2015) have explored vertical  
230 profile retrievals from TCCON, but there is not yet an operational product.

231

## 232 **3.0 LMT and U theoretical basis**

233 In Section 3.1, equations are presented describing the sensitivity and errors  
234 of the new products. In Section 3.2, a simulation is shown of what GOSAT is  
235 expected to see from space using the developed equations and aircraft  
236 profiles from the Southern Great Plains (SGP) aircraft site.

237

## 238 **3.1 Equations describing sensitivity and errors**

239 The ACOS retrievals (O'Dell et al., 2012) utilize an optimal estimation  
240 approach with a priori constraints (Rodgers, 2000). It is common practice to  
241 represent the state parameter to be retrieved on an altitude grid that is finer  
242 than the altitude resolution of the instrument (e.g., Bowman et al., 2006;  
243 Deeter et al., 2003; von Clarmann et al., 2003). A major advantage of this  
244 approach is that it allows the calculation of diagnostics, such as averaging  
245 kernels, which can be used to characterize the sensitivity of the  
246 measurement. Constraints (regularization) must be applied in order to  
247 stabilize the retrieval (e.g., Rodgers, 2000; Tikhonov, 1963; Twomey, 1963;  
248 Steck and von Clarmann, 2001; Kulawik et al., 2006). The constraints  
249 include a constraint vector and a constraint matrix, which may be chosen  
250 to constrain absolute values and/or the shape of the retrieved result.

251

252 In the ACOS processing, CO<sub>2</sub> is first retrieved as a 20-level profile, which  
253 averages 1.6 degrees of freedom (DOF) with about 0.8 DOF below 2.5 km  
254 above the surface (levels 16-20, where level 20 is the surface), and 0.8 DOF  
255 above 2.5 km (levels 1-15). This intermediate profile has significant  
256 altitude-dependent biases and cannot be used scientifically as-is, but rather  
257 this profile is compacted to a single column quantity, XCO<sub>2</sub> as the final step  
258 in the ACOS processing. In this work, we post-process the ACOS-GOSAT  
259 intermediate profile to calculate and characterize the partial column  
260 represented by levels 16-20, which is named LMT\_XCO<sub>2</sub> or LMT for short,



261 and the partial column represented by levels 1-15, which is named  $U_{XCO_2}$   
 262 or  $U$  for short.

263

264 The equation for the linear estimate of  $\mathbf{x}$ , the retrieved  $CO_2$  profile (Connor  
 265 et al., 2008; Rodgers, 2000) is:

266

$$267 \quad \hat{\mathbf{x}} = \mathbf{x}_a + \mathbf{A}_{xx}(\mathbf{x}_{true} - \mathbf{x}_a) + \mathbf{A}_{xy}(\mathbf{y} - \mathbf{y}_a) + \mathbf{G}_x \boldsymbol{\varepsilon} \quad (1)$$

268

269 where  $\hat{\mathbf{x}}$  is the retrieved  $CO_2$  profile with size  $n_{CO_2}$  (20 for ACOS-GOSAT),  
 270  $\mathbf{x}_{true}$  is the true value,  $\mathbf{A}_{xx}$  is the  $n_{CO_2} \times n_{CO_2}$   $CO_2$  profile averaging kernel, and  
 271  $\mathbf{A}_{xy}(\mathbf{y} - \mathbf{y}_a)$  is the cross-state error representing the propagation of error from  
 272 non- $CO_2$  retrieved parameters  $\mathbf{y}$  (aerosols, albedo, etc., size 26 for ACOS-  
 273 GOSAT as there are 26 non- $CO_2$  retrieved parameters) into retrieved  $CO_2$ ,  
 274 size  $n_{interf} \times n_{CO_2}$ ; and  $\mathbf{G}_x \boldsymbol{\varepsilon}$  is the measurement error.

275

276 The pressure weighting function, " $\mathbf{h}$ " (size  $n_{CO_2}$ ) is used to convert the  
 277 retrieved  $CO_2$  profile to  $XCO_2$  by tracking each level's contributes to the  
 278 column quantity.

279

$$280 \quad \mathbf{h}_{xco_2} = [0.026 \ 0.052 \ 0.052 \ 0.052 \ \dots \ 0.052 \ 0.052 \ 0.052 \ 0.026] \quad (2a)$$

281

282 The sensitivity to the top or bottom levels is half other levels, as these levels  
 283 contribute to only one layer, rather than two adjacent layers. The GOSAT  
 284 levels are chosen such that the pressure weighting is the same for all layers  
 285 and the same for all observations.

286

287 The LMT pressure weighting function is obtained by starting with the  
 288 pressure weighting function for  $XCO_2$ , setting levels 1-15 to zero, then  
 289 normalizing so that the sum of all entries adds to 1. For the  $U$  pressure  
 290 weighting function, levels 16-20 are set to zero, then the vector is  
 291 normalized so that the sum is 1. The LMT and  $U$  pressure weighting  
 292 functions are:

293

$$294 \quad \mathbf{h}_{LMT} = [0 \ 0 \ 0 \ 0 \ \dots \ 0 \ 0.22 \ 0.22 \ 0.22 \ 0.22 \ 0.11] \quad (2b)$$

$$295 \quad \mathbf{h}_U = [0.035 \ 0.069 \ 0.069 \ \dots \ 0.069 \ 0.069 \ 0 \ 0 \ 0 \ 0] \quad (2c)$$

296

297 To calculate  $XCO_2$ , the equation is:

298

$$299 \quad XCO_2 = \mathbf{h}_{xco_2} \cdot \hat{\mathbf{x}} \quad (3)$$

300

301 The fraction of total air in each of the partial columns are:

302

$$303 \quad f_{xco_2} = 1 \quad (4a)$$



$$304 \quad f_{\text{LMT}} = 0.23446 \quad (4b)$$

$$305 \quad f_{\text{U}} = 0.76554 \quad (4c)$$

306

307 Combining Eqs. 1, 2a, and 3, the XCO<sub>2</sub> estimate is:

308

$$309 \quad (X\hat{C}O_2) = (XCO_2)_a + \mathbf{h}_{XCO_2} \mathbf{A}_{xx} (\mathbf{x}_{true} - \mathbf{x}_a) + \mathbf{h}_{XCO_2} \mathbf{A}_{xy} (\mathbf{y} - \mathbf{y}_a) + \mathbf{h}_{XCO_2} \mathbf{G}_x \quad (5a)$$

$$310 \quad (X\hat{C}O_2) = (XCO_2)_a + \mathbf{a}_{xx} (\mathbf{x}_{true} - \mathbf{x}_a) + \mathbf{a}_{xy} (\mathbf{y} - \mathbf{y}_a) + \mathbf{g}_x \boldsymbol{\varepsilon} \quad (5b)$$

311

312 where  $\mathbf{a}_{xx}$  is the column averaging kernel,  $\mathbf{a}_{xx} = \mathbf{h}_{XCO_2}^T \mathbf{A}_{xx}$  (see Appendix A of  
 313 Connor, 2008).

314

315 Similarly, to calculate the linear estimate for the 2-vector [LMT, U], Equation  
 316 1 is multiplied by the 2 x  $n_{CO_2}$  pressure weighting function,  $\mathbf{h} = [\mathbf{h}_{\text{LMT}}, \mathbf{h}_{\text{U}}]$ :

317

$$318 \quad \begin{pmatrix} L\hat{M}T \\ \hat{U} \end{pmatrix} = \begin{pmatrix} LMT \\ U \end{pmatrix}_a + \mathbf{h} \mathbf{A}_{xx} (\mathbf{x}_{true} - \mathbf{x}_a) + \mathbf{h} \mathbf{A}_{xy} (\mathbf{y} - \mathbf{y}_a) + \mathbf{h} \mathbf{G}_x \boldsymbol{\varepsilon} \quad (6a)$$

$$319 \quad \begin{pmatrix} L\hat{M}T \\ \hat{U} \end{pmatrix} = \begin{pmatrix} LMT \\ U \end{pmatrix}_a + \mathbf{a}_{xx} (\mathbf{x}_{true} - \mathbf{x}_a) + \mathbf{a}_{xy} (\mathbf{y} - \mathbf{y}_a) + \mathbf{g}_x \boldsymbol{\varepsilon} \quad (6b)$$

320

321 where now  $\mathbf{a}_{xx} = [\mathbf{h}_{\text{LMT}}, \mathbf{h}_{\text{U}}] \mathbf{A}_{xx}$ , a 2 x  $n_{CO_2}$  matrix,  $\mathbf{a}_{xy} = [\mathbf{h}_{\text{LMT}}, \mathbf{h}_{\text{U}}] \mathbf{A}_{xy}$ , a 2x  
 322  $n_{interf}$  matrix, and  $\mathbf{g}_x = [\mathbf{h}_{\text{LMT}}, \mathbf{h}_{\text{U}}] \mathbf{G}_x$ , a 2x $n_s$  matrix, where  $n_s$  are the number  
 323 of spectral points.

324

325 The last two terms in Eq. 6 represent the cross-state and measurement  
 326 error, respectively, and are often jointly called the observation error  
 327 (Worden et al., 2004). The error in [LMT, U] is estimated by taking the

328 covariance of  $\begin{pmatrix} L\hat{M}T \\ \hat{U} \end{pmatrix} - \begin{pmatrix} LMT \\ U \end{pmatrix}_{True}$ . The errors can be calculated either from

329 taking the covariance (6a) or from (6b). The covariance of (6a) has a fairly  
 330 simple form, in terms of the standard definitions of the error covariances for  
 331 the full profile,  $\mathbf{S}_{interf}$ , and  $\mathbf{S}_{meas}$ , which are included in the ACOS-GOSAT  
 332 ancillary products, and  $\mathbf{S}_{smoothing}$  can be calculated from the standard  
 333 equation,  $\mathbf{S}_{smoothing} = (\mathbf{I} - \mathbf{A}) \mathbf{S}_a (\mathbf{I} - \mathbf{A})^T$  (Rodgers, 2000), with  $\mathbf{A}$  the  $n_{CO_2} \times n_{CO_2}$   
 334 CO<sub>2</sub> profile averaging kernel and  $\mathbf{S}_a$  the a priori covariance, both included in  
 335 the ACOS-GOSAT products.

336

$$337 \quad \sigma_{[LMT,U]} = \mathbf{h} \mathbf{S}_{smoothing} \mathbf{h}^T + \mathbf{h} \mathbf{S}_{interfer} \mathbf{h}^T + \mathbf{h} \mathbf{S}_{meas} \mathbf{h}^T \quad (7a)$$

$$338 \quad = \begin{pmatrix} \mathbf{h}_{lmt}^T \mathbf{S}_{smooth} \mathbf{h}_{lmt} & \mathbf{h}_{lmt}^T \mathbf{S}_{smooth} \mathbf{h}_U \\ \mathbf{h}_U^T \mathbf{S}_{smooth} \mathbf{h}_{lmt} & \mathbf{h}_U^T \mathbf{S}_{smooth} \mathbf{h}_U \end{pmatrix} + \begin{pmatrix} \mathbf{h}_{lmt}^T \mathbf{S}_{obs} \mathbf{h}_{lmt} & \mathbf{h}_{lmt}^T \mathbf{S}_{obs} \mathbf{h}_U \\ \mathbf{h}_U^T \mathbf{S}_{obs} \mathbf{h}_{lmt} & \mathbf{h}_U^T \mathbf{S}_{obs} \mathbf{h}_U \end{pmatrix} \quad (7b)$$





$$= \begin{pmatrix} \sigma_{LMT}^2 & \sigma_{LMT} \sigma_U corr \\ \sigma_{LMT} \sigma_U corr & \sigma_U^2 \end{pmatrix} \quad (7c)$$

340

341 The resulting error covariance  $\sigma_{[LMT,U]}$  is a 2x2 matrix, where the diagonals  
 342 are the square of the predicted error for each parameter, and the off  
 343 diagonals also depend on the correlated errors between these parameters.  
 344 Table 1 shows the predicted errors for LMT, U, and the error correlation  
 345 between LMT and U. The predicted errors in Table 1 are larger than the  
 346 actual errors, seen in Tables 2 and 3; and the error for averaged  
 347 observations is estimated in section 4.1.1. It is worth noting that the *a*  
 348 *priori* errors are much larger for LMT and U, at 34 and 9 ppm, respectively,  
 349 than the posterior errors, indicating that these quantities are largely  
 350 unconstrained by the retrieval's prior assumption.

351

352 Through the same process as Eqs 6-7, the XCO<sub>2</sub> error is:

353

$$\sigma_{XCO_2} = \mathbf{h}_{XCO_2}^T \mathbf{S}_{smooth} \mathbf{h}_{XCO_2} + \mathbf{h}_{XCO_2}^T \mathbf{S}_{obs} \mathbf{h}_{XCO_2} \quad (8)$$

355

356 XCO<sub>2</sub> can also be calculated as a function of LMT and U, and the XCO<sub>2</sub> errors  
 357 can be calculated as a function of the errors in [LMT, U]. These are shown in  
 358 Eq. 9.

359

$$XCO_2 = f_{lmt} LMT\_CO_2 + f_u U\_CO_2 \quad (9a)$$

361

$$\sigma_{XCO_2} = \sqrt{(f_{lmt} \quad f_u) \begin{pmatrix} \sigma_{lmt}^2 & \sigma_{lmt} \sigma_u corr \\ \sigma_{lmt} \sigma_u corr & \sigma_u^2 \end{pmatrix} \begin{pmatrix} f_{lmt} \\ f_u \end{pmatrix}} \quad (9b)$$

363

$$\sigma_{XCO_2} = \sqrt{0.23^2 \sigma_{lmt}^2 + \sigma_u^2 0.77^2 + 2 * 0.77 * 0.23 \sigma_{lmt} \sigma_u corr} \quad (9c)$$

365

366 where  $f_{LMT}$  and  $f_U$  are the air masses for the LMT and U partial columns  
 367 (0.236, 0.764), respectively,  $\sigma_{lmt}$  is the error for LMT, and *corr* is the error  
 368 correlation between LMT and U.

369

370 The normalized column averaging kernel is used to see the sensitivity of the  
 371 column to the true state at different levels, with a value of 1 meaning  
 372 perfect sensitivity, and a value of 0 meaning no sensitivity. The normalized  
 373 column averaging kernel is the column averaging kernel,  $\mathbf{a}$ , divided by the  
 374 pressure weighting function for each layer,  $\mathbf{h}_{XCO_2}$ , and multiplied by the  
 375 fraction of air in the partial column.

376

$$\mathbf{a\_norm}_{LMT} = (\mathbf{h}_{LMT} \mathbf{A}_{CO_2}) / \mathbf{h}_{XCO_2} * f_{LMT} \quad (10a)$$

$$\mathbf{a\_norm}_U = (\mathbf{h}_U \mathbf{A}_{CO_2}) / \mathbf{h}_{XCO_2} * f_U \quad (10b)$$

377



379

380 Figure 3 shows the normalized column averaging kernels for LMT, U, and  
381 XCO<sub>2</sub> for land and ocean scenes. Although the LMT partial column sums the  
382 5 levels within about 2.5 km of the ground, the LMT has some sensitivity to  
383 the true state at all 20 levels because the GOSAT radiances are not able to  
384 fully resolve between CO<sub>2</sub> within the surface to 2.5 km versus above this.  
385 As expected, the sensitivity for LMT plus U is equal to the sensitivity for  
386 XCO<sub>2</sub>, and the sensitivity for LMT is weighted to the surface whereas the  
387 sensitivity for U is weighted to the top of the atmosphere. The negative  
388 averaging kernels for LMT in the stratosphere are partially a consequence of  
389 the ACOS prior constraint, which allows no stratospheric variability. Actual  
390 stratospheric variability is transferred to the closest levels that are allowed  
391 to vary, and the surface compensates for the radiance error induced by this,  
392 resulting in a negative sensitivity of the LMT to the true state in the  
393 stratosphere. If the stratospheric truth matches that of the *a priori*, then  
394 there will be no propagation of error into LMT or U. The averaging kernels  
395 shown in Fig. 3 are similar to those calculated for TCCON in Figure 2 of  
396 Connor et al. (2015).

397

### 398 **3.2 Seasonal behavior of LMT, U, and XCO<sub>2</sub> estimated using *only*** 399 **aircraft measurements and GOSAT sensitivity (no GOSAT** 400 **observations)**

401 This section answers the following questions: (1) Do U and LMT have unique  
402 seasonal signatures? (2) How much of the XCO<sub>2</sub> variability is due to LMT  
403 versus U variability (3) How much does the prior influence the LMT and U  
404 retrievals?

405

406 This section uses simulated GOSAT retrievals using the linear estimate, Eqs.  
407 5 and 6, given the aircraft in situ profiles at the SGP site (37N, 95W), the  
408 GOSAT prior, and the GOSAT averaging kernels. Using this analysis, the  
409 importance of the prior is assessed by using either a flat prior or the GOSAT  
410 prior in Eqs. 5 and 6. We assess how much LMT and U contribute to the  
411 variations seen in XCO<sub>2</sub> using the variability of the LMT and U partial  
412 columns combined with the weighting each has in the full column. The  
413 seasonal cycles of each partial column are studied by converting all aircraft  
414 measurements to lie between 2012 and 2013 by applying a 2 ppm/year  
415 secular trend, and averaging by month. This method was used rather than  
416 fitting the aircraft observations using the NOAA CCGCRV to estimate the  
417 seasonal cycle shape because the aircraft observations are not sufficiently  
418 smooth to result in a consistent fit.

419 Figure 4 shows the estimates of LMT, U, and XCO<sub>2</sub> using SGP aircraft profiles  
420 calculated as described above. There is significant variability in the  
421 individual aircraft measurements, seen in panel (a) but this is smoothed out  
422 on monthly timescales, seen in the remaining panels. The dashed lines in



423 panel a represent fits using the NOAA fitting software CCGCRV. The U  
424 partial column is rarely more than 1 ppm different from the fit, whereas LMT  
425 can be up to 5 ppm different (e.g. see summer, 2009; January, 2010;  
426 Summer, 2011).

427

428 Figure 4 (b) and (c) show the difference between simulated retrievals with  
429 the GOSAT a priori (b) versus a flat a priori (c). The patterns are very  
430 similar, indicating that the signal is primarily coming from the data rather  
431 than the prior, with standard deviations of 0.8 ppm for LMT and 0.3 ppm for  
432 U (these changes are fully characterized when applying the GOSAT prior to  
433 the aircraft true profile with the specified a priori vector).

434

435 Figure 4, panel (d) shows U versus XCO<sub>2</sub>. At first glance these look the  
436 same, but by comparing panel (d) and (b), the XCO<sub>2</sub> deviations from U are  
437 towards LMT. The seasonal variabilities of XCO<sub>2</sub>, LMT, and U (maximum  
438 minus minimum), are 3.3 ppm, 4.8 ppm, and 3.3 ppm, respectively. Note  
439 that the seasonal variations in LMT and U have a 0.56 correlation. A  
440 straightforward calculation of variation \* airfraction (Eq. 4) show that the  
441 fraction of variation of XCO<sub>2</sub> resulting from variations in LMT is  
442 approximately 30%, and the fraction of the variation in XCO<sub>2</sub> coming from U  
443 variation is roughly 70%. So even though LMT has more variability, U has  
444 the much larger impact on XCO<sub>2</sub> due to the fact that the full column is 77%  
445 LMT. A similar calculation at Park Falls, where the LMT seasonal cycle is 20  
446 ppm and the U seasonal cycle is 5 ppm finds 45% of the seasonal variability  
447 in XCO<sub>2</sub> results from U and 55% from LMT at Park Falls (46N).

448

449 Figure 4 indicates that LMT and U do have unique seasonal cycles which  
450 result from the data rather than the prior. The LMT partial column, which  
451 contributes to 30% of the variations observed in XCO<sub>2</sub>, has a much larger  
452 seasonal variability than the U partial column or the XCO<sub>2</sub> column, and  
453 earlier seasonal cycle maximums and minimums.

454

#### 455 **4.0 Methods**

456 We test the sensitivity of the new products to surface fluxes using back-  
457 trajectory footprints in Section 4.1. Section 4.2 discusses how GOSAT is  
458 compared to aircraft. Sections 4.3-5.6 describe the bias correction, how the  
459 aircraft data is extended to the full atmosphere and the coincidence criteria.

460

#### 461 **4.1 Sensitivity of the LMT and U partial columns to surface fluxes**

462 To compare LMT and U sensitivity to surface fluxes, we look at 10-day back-  
463 trajectory footprints created using WRF-STILT (Nehrkorn et al., 2010). The  
464 "footprint" for an observation is a map of the surface locations to which an  
465 observation is sensitive. Footprints are created for each of the 20 GOSAT  
466 levels, then convolved with the LMT and U averaging kernels. The averaging



467 kernel estimates the sensitivity of the GOSAT measurement of each quantity  
468 to the true state at each level. Footprint maps are created which show the  
469 sensitivity of each type of GOSAT observation to sources and sinks. This  
470 was done for 10 GOSAT observations in the Amazon. The distance for the  
471 nearest 10% of footprints is 260 km for LMT and 790 km for U. It is likely  
472 that there is also a very long tail in the U sensitivity, based on the work of  
473 Liu et al. (2015) and Feng et al. (2016).

474

#### 475 **4.2 Comparisons to aircraft**

476 The correct way to validate GOSAT estimates of [LMT, U] is to compare the  
477 GOSAT observations to an estimate of what GOSAT should observe, given its  
478 sensitivity, when the true atmospheric state is set to the aircraft CO<sub>2</sub> profile  
479 using Eq. 6. The agreement should be within the GOSAT observation error,  
480 as the smoothing term's effects on the comparison are removed by the  
481 application of the GOSAT averaging kernel to the validation data.

482

#### 483 **4.3 GOSAT bias correction**

484 The GOSAT standard XCO<sub>2</sub> product has regional biases and errors which can  
485 be partially corrected using jointly retrieved parameters, pre-filters, or  
486 radiance properties, e.g. the ratio of the signal in the strong vs. weak band,  
487 retrieved albedo slopes or values, retrieved aerosol slopes or values; and  
488 through post-processing screening, e.g. removing fits where the difference  
489 in the retrieved versus prior surface pressure is greater than 4 hPa ( $\sigma$ ). We  
490 apply the same techniques to the LMT partial column in Appendix A which is  
491 briefly described here. After LMT is corrected, the corrected U partial  
492 column is set using Eq. 9a, so that XCO<sub>2</sub> is consistent with LMT and U.

493

494 To correct the LMT partial column, a set of pairs of "true" and "retrieved"  
495 values is compiled, using validation data. GOSAT minus true is plotted  
496 versus various GOSAT parameters described in Appendix A, and if a slope is  
497 found for GOSAT error versus a parameter, a correction is applied. The  
498 robustness of the correction is tested by applying the correction on data  
499 withheld from the fit, as described in Appendix A. Following the initial bias  
500 correction, GOSAT LMT is compared for closely occurring ocean and land  
501 pairs; the a constant bias term is added to the land bias correction so that  
502 land and ocean, on average, are consistent.

503

#### 504 **4.4 Coincidence criteria**

505 "Geometric criteria", defined as  $\pm 3$  degrees latitude,  $\pm 5$  degrees longitude  
506  $\pm 1$  week time are used to select coincident GOSAT observations for  
507 particular sites. 5 degrees latitude/longitude, 1 hour has previously be used  
508 for GOSAT criteria (Kulawik et al., 2016), however this did not yield enough  
509 matches for aircraft profiles. With the above criteria, the total matches  
510 range from 64 (PFA) to 4800 (SGP), with median 430, which is



511 approximately 9/month. A tight spatial criteria was selected to best capture  
512 the seasonal cycle at a given location, especially for land where spatial  
513 variability is large. Because aircraft and surface observations are more  
514 infrequent than TCCON, extended time was used for the comparisons to  
515 obtain sufficient comparison data. Other methods that were tried were  
516 dynamic coincidence criteria (Wunch et al., 2011b) which considers a larger  
517 area (+- 10 degrees latitude, +- 30 degrees longitude) but also matches  
518 atmospheric temperature, and a variant of Basu criteria (Guerlet et al.,  
519 2013), which used dynamic coincidences which had model-model differences  
520 less than 0.5 ppm. All three criteria gave similar results overall, with  
521 different criteria performing better at different stations, but no clear overall  
522 best criteria. For HIPPO data, which mainly tests latitude gradients over  
523 ocean, the dynamic coincidence approach was used following Frankenberg et  
524 al. (2016)

525

#### 526 **4.5 Extension of the aircraft profile**

527 The aircraft measurements go from the surface to between 5.5 km to 8 km  
528 for most ESRL land to 9-13 km for HIPPO observations. As GOSAT LMT, U,  
529 and XCO<sub>2</sub> have sensitivity above 5.5 km and even above 13 km, as seen in  
530 the averaging kernel shown in Fig. 3, the aircraft profile needs to be  
531 extended from the top measurement to the top of the atmosphere. Four  
532 different methods of extension were tested: extending with the GOSAT  
533 prior, extending the top aircraft measurement through the tropopause and  
534 extending with the GOSAT prior above this, extending with the CT2015  
535 model, and extending the top aircraft measurement through the tropopause  
536 and extending with the CT2015 model above this. The different extensions  
537 mainly had an effect on the overall LMT, U, and XCO<sub>2</sub> biases, rather than the  
538 standard deviation, with a spread of 0.4 ppm, as seen in Table A4. The  
539 extension that was used in the rest of the paper is extending the top aircraft  
540 measurement through the tropopause and extending with the CT2015 model  
541 above this.

542

#### 543 **5. GOSAT results**

544 Figure 5 shows GOSAT comparisons for LMT and U versus the aircraft  
545 measurements at the SGP site at 37N, 95W which can be compared to the  
546 simulated results shown in Fig. 4. The GOSAT LMT and U products show the  
547 same seasonal patterns as seen in the aircraft data. Figure 5b shows  
548 CarbonTracker matched to GOSAT (CT@GOSAT) and CarbonTracker  
549 matched to the aircraft measurements (CT@aircraft). The difference of  
550 CT@GOSAT and CT@aircraft estimates the co-location error. Large  
551 differences are seen between CT@GOSAT and CT@aircraft in early 2010,  
552 Summer, 2010, and Summer, 2011. In Fig. 5c, the seasonal cycle is shown  
553 by transforming all data to lie within 2012 using 2 ppm/year adjustment to  
554 CO<sub>2</sub>. There are systematic differences seen in the drawdown, which is



555 underestimated by GOSAT. However, when months that have differences of  
556 (CT@GOSAT -CT@aircraft) more than 2.5 ppm are removed, Figure 5d  
557 shows agreement within the GOSAT predicted errors between GOSAT and  
558 aircraft.

559

560 GOSAT U improves over the a priori for real (Figs. 5c-d) and in simulated  
561 (Fig. 4b) results. The black (aircraft) vs. blue (GOSAT) in Fig. 5c shows  
562 much better agreement in July-November than prior (green) vs. black  
563 (aircraft). The bias seen in the U partial column versus the aircraft U  
564 estimate is also found in XCO<sub>2</sub> versus the aircraft.

565

### 566 **5.1 Summary of comparisons to all validation data**

567 GOSAT LMT, U, and XCO<sub>2</sub> are compared to aircraft profiles, where the  
568 aircraft profile has the GOSAT averaging kernel applied so that the  
569 sensitivity is considered. The comparison locations are shown in Fig. 2.  
570 More detailed comparisons, showing results for each location and/or  
571 campaign, are shown in Appendix B.

572

573 Table 2 shows the biases with respect to aircraft data and Table 3 shows the  
574 standard deviation with respect to aircraft, for single and averaged  
575 observations. The bias or standard deviation is calculated for every site (or  
576 campaign). The mean represents the average of all site means, and the ±  
577 represents the standard deviation of all the sites (or campaigns). The  
578 variability of the bias by location or time is a key metric in the data quality.  
579 Biases that vary by season or location are the biggest detriment of use of  
580 satellite data (or any other type), as the assimilation will attribute these  
581 biases to spurious fluxes.

582

583 The co-location error is estimated by comparing CarbonTracker to itself at  
584 the satellite location/time and CarbonTracker at the aircraft location/time.  
585 For the ocean surface sites, a vertical co-location error is estimated by  
586 comparing CarbonTracker with the LMT averaging kernel to CarbonTracker  
587 at the surface. In Tables 2-4, the top entry in the ocean surface ct\_ct  
588 difference is from discrepancies in horizontal location and time. The bottom  
589 entry is the ct\_ct difference between the CarbonTracker LMT quantity and  
590 CarbonTracker at the surface.

591

#### 592 **5.1.1 Bias**

593 In Table 2, the "ct\_ct bias" is the estimate of the co-location bias; it is the  
594 mean difference between CarbonTracker at the satellite location/time and  
595 CarbonTracker at the aircraft location/time. The ct\_ct bias is largest for  
596 aircraft land, with an overall bias of -0.6 ppm and bias variability of 0.7 ppm.  
597 This gives an approximate best case of what could be achieved by GOSAT-  
598 AIRCRAFT comparisons. An investigation of the -2 ppm ct\_ct bias at CAR in



599 July, during the drawdown finds that the GOSAT observations are always  
600 taken 3-4 hours later than the aircraft in July. The CarbonTracker model  
601 estimates the effect of +3 hours as resulting in a -2 ppm change. The ct\_ct  
602 bias reflects spatial, diurnal, and seasonal co-location errors. Taking out the  
603 5 sites that have errors > 0.5 ppm (see Appendix B, table b): WBI, BNE,  
604 CAR, HIL, and CMA, reduces the ct\_ct bias to  $-0.2 \pm 0.3$  ppm.  
605

606 In Table 2, the "true mean by site/campaign" is the mean value averaged by  
607 location (or campaign number). The  $\pm$  represents the standard deviation of  
608 the mean by location (or campaign number). The GOSAT retrieval must  
609 improve on the  $\pm$  at the very least to provide information on the  
610 atmospheric state. The GOSAT a priori bias represents how well the GOSAT  
611 prior does. The GOSAT prior improves over the true variability on land but  
612 not for ocean cases for LMT. For U, the a priori variability to true is the  
613 same size as the true variability. The "GOSAT bias" is the bias of the  
614 retrieved GOSAT values. Comparing to the GOSAT prior, there is  
615 improvement in all entries of the absolute bias, except XCO<sub>2</sub> for ESRL ocean,  
616 and U, XCO<sub>2</sub> for AJAX. Issues with both U and XCO<sub>2</sub> suggests a possible  
617 issue with the profile extension above the aircraft. The improvement in the  
618 GOSAT  $\pm$  bias occurs in all ocean comparisons and in LMT land. For ESRL  
619 land, GOSAT LMT has an overall bias of -0.3 ppm and bias variability of 1.0  
620 ppm. If the 5 stations with large ct\_ct variability are taken out, the bias  
621 decreases to  $-0.3 \pm 0.7$  ppm.  
622

623 The location-dependent bias is important because this bias variability will be  
624 attributed to phantom fluxes. The bias variability is 0.5 (1.0) ppm for  
625 GOSAT LMT, 0.2 (0.9) ppm for U, and 0.4 (0.9) for XCO<sub>2</sub> ocean (land). The  
626 LMT location dependent bias is no worse than the XCO<sub>2</sub> location dependent  
627 bias, whereas the LMT signals are much more variable than XCO<sub>2</sub>. The bias  
628 variability for XCO<sub>2</sub> and U are possibly too high due to uncertainty of the  
629 aircraft profile extension because the bias variability is much larger than the  
630 0.3 ppm seen in Kulawik et al. (2016) versus TCCON. The variability of the  
631 LMT ct\_ct bias is 0.7 ppm, and when the 5 sites with ct\_ct co-location error  
632 larger than 0.5 ppm are taken out, the GOSAT LMT bias variability drops to  
633 0.7 ppm. Taking out sites with large ct\_ct biases for XCO<sub>2</sub> does not improve  
634 the GOSAT XCO<sub>2</sub> bias variability. Taking out the top 4 GOSAT bias outliers  
635 results in a GOSAT bias variability of 0.5 ppm for the remaining sites,  
636 however these 4 sites are not the same sites where LMT has bias issues, nor  
637 are they sites where ct\_ct XCO<sub>2</sub> shows a large bias.  
638

### 639 5.1.2 Standard deviation

640 Table 3 shows standard deviations of key quantities versus aircraft data.  
641 The co-location standard deviation, which is estimated using the standard  
642 deviation of CarbonTracker at the satellite location/time minus



643 CarbonTracker at the aircraft location/time, is less than 0.3 ppm for aircraft  
 644 ocean, 2.1 ppm for LMT land, 0.5 ppm for U land, and 0.8 ppm for XCO<sub>2</sub>  
 645 land. The surface ocean has 1.0 ppm co-location error, also including the  
 646 vertical co-location. The AJAX comparisons, which are primarily from GOSAT  
 647 underflights, has a co-location error half that of the ESRL land matches,  
 648 which have coincidence criteria of 7 days, and 3-5 degrees.

649  
 650 The next entry is the predicted error, given by Eqs. 7 and 9, which is on the  
 651 order of 4.5 ppm for LMT, 1.7 ppm for U, and 0.7 ppm for XCO<sub>2</sub>. The actual  
 652 standard deviation of GOSAT versus aircraft, however, is about half that for  
 653 LMT and U, and double the predicted error for XCO<sub>2</sub>. This is discussed in  
 654 Section 5.1.5.

655  
 656 The next entry, "true variability" shows how much the different partial  
 657 columns vary seasonally. The variability of LMT for land, at 5.4 ppm, is  
 658 about double that of U or XCO<sub>2</sub> (at 2.0 and 2.5 ppm, respectively), and the  
 659 variability for ESRL ocean, at 1.1 ppm, about 50% larger than U, XCO<sub>2</sub> at  
 660 0.8 ppm.

661  
 662 The prior standard deviation (n=15), and GOSAT standard deviation (n=15)  
 663 look at the error of averaged GOSAT values, which is important for  
 664 assimilation. Similarly to Kulawik et al. (2016), the GOSAT error does not  
 665 drop off as the inverse square root of the number of observations, like it  
 666 would if the error were fully random. The error for 15 observation averages  
 667 is about 0.4 times that of 1 observation for land, with a similar factor for all  
 668 quantities; and about 0.5 times that of 1 observation for ocean, similarly for  
 669 all quantities. Note that the co-location error has been subtracted out (in  
 670 quadrature) for both the a priori and GOSAT errors.

671  
 672 The standard deviations for LMT, U, and XCO<sub>2</sub> improve over the prior for  
 673 land cases but improve only marginally or do not improve over ocean. The  
 674 location-dependent bias, however, does show improvement for LMT and U in  
 675 Table 2. For surface ocean sites, which are only compared to LMT, the  
 676 improvement over the prior is much better, mainly because the prior is not  
 677 very good at these sites.

678  
 679 **5.1.3 Errors separated into co-location, random, and correlated error**

680 The errors between aircraft and GOSAT observations can be parametrized by  
 681 the number of GOSAT observations that are averaged. Kulawik et al. (2016)  
 682 found the form in Eq. 11 matched well to the observed errors.

683  
 684 
$$error = \sqrt{(a^2 + b^2 / n)} \quad (11)$$

685 
$$error = \sqrt{(\varepsilon_{coloc}^2 + a_o^2 + b^2 / n)} \quad (12)$$





686

687 where  $n$  are the number of GOSAT observations that are averaged (all of the  
688 averaged observations match a single aircraft measurement),  $a$  is error that  
689 does not reduce with averaging, and  $b$  is the random error.  $a$  is further split  
690 into co-location error,  $\varepsilon_{coloc}$ , plus  $a_o$ , the correlated error in Eq. 12. Correlated  
691 error means that no matter how many observations are taken, this error  
692 does not reduce, and can be due to interferences or spectroscopy in  
693 combination with attributes specific to different locations and times.

694

695 The co-location error is the error resulting from imperfect matching of the  
696 aircraft and satellite observations, and is approximated by the standard  
697 deviation of the CarbonTracker model at the validation location and time and  
698 the model at the satellite observation location and time, and is tabulated in  
699 Table 4. This term, as seen in Table 4, is comparable to or even larger than  
700  $a$  for LMT land cases. Some co-location schemes (e.g. as implemented by S.  
701 Basu described in Guerlet et al. (2013)) use the model-model differences to  
702 select the best satellite observations to match validation data. Equation 11  
703 is used to determine  $a$  and  $b$ , and then  $a_o$  is calculated from  $a$  and  $\varepsilon_{coloc}$ .

704

705 The co-location error is subtracted from the correlated error, to try to  
706 remove the effect of co-location on the error estimate. The three quantities  
707 from Eq. 12 are shown in Table 4. For LMT the co-location error is about the  
708 same size as the correlated error for ocean, and the co-location error is  
709 larger than correlated error for land. For U and XCO<sub>2</sub>, the correlated errors  
710 are larger than the co-location error for ocean, and comparable for land.

711

#### 712 **5.1.4 Comparison of XCO<sub>2</sub> results to previous results**

713 We compare GOSAT XCO<sub>2</sub> comparisons to the previous validations using  
714 TCCON (Wunch et al., 2011b; Kulawik et al., 2016) and HIPPO observations  
715 (Frankenberg et al., 2016). The GOSAT comparisons to HIPPO in  
716 Frankenberg et al. (2016) were for at least 6 averages and did not subtract  
717 co-location error (which is only 0.1 ppm over ocean). Using Eq. 12 and  
718 Table 4, we find that the XCO<sub>2</sub> error for  $n=6$  is 0.43 ppm, in agreement with  
719 0.45 from Frankenberg et al. (2016). We would expect the same result, as  
720 we are comparing to the same dataset with the same coincidence criteria.  
721 Without co-location error, the XCO<sub>2</sub> from  $n=6$  is 0.42 ppm. For ESRL land,  
722 several quantities in Tables 2-4 can be directly compared to previous  
723 GOSAT/TCCON validation: the co-location error (0.8 ppm) is larger than co-  
724 location for geometric coincidence (0.4 ppm) but smaller than for dynamic  
725 coincidence (0.9 ppm) from Kulawik et al. (2016). This makes sense as  
726 Kulawik et al. (2016) had a 1 hour coincidence with TCCON whereas 7 days  
727 is used in this paper, since aircraft measurements are sparser in time than  
728 TCCON observations.  $a_o$  and  $b$  values of  $0.7\pm 0.5$  ppm and  $1.6\pm 0.2$  ppm in



729 this work are consistent with  $0.8 \pm 0.2$  ppm and  $1.6 \pm 0.1$  ppm, for a  
730 (corrected) and b, respectively, from Kulawik et al. (2016) Table 2.  
731 Additionally, the predicted error of  $0.9 \pm 0.1$  which is a factor of 1.9 less than  
732 the actual error of  $1.7 \pm 0.4$  are identical to the values and relative sizes of  
733 predicted versus actual error in Kulawik et al. (2016) at the end of section  
734 3.1. Kulawik et al. (2016) estimated that the XCO<sub>2</sub> location-dependent bias  
735 was 0.3 (after removing outlying stations north of 50N and locally-influenced  
736 stations).

737

738 As discussed in Section 5.1.1, the location-dependent bias found in Kulawik  
739 et al. (2016) versus TCCON sites was 0.3 (after removing outlying stations  
740 north of 60N and locally-influenced stations). In this paper, we find this  
741 variability to be 1.0 ppm. One reason for the discrepancy could be from the  
742 extension of the profile above the aircraft measurement (about 5-6 km).  
743 However, as seen in Table A4, extension of the aircraft profile by 4 different  
744 methods did not make more than 0.1 ppm difference in the bias variability of  
745 U. Another possible cause for the discrepancy is that GOSAT has been  
746 extensively tested against TCCON and issues that show up at TCCON  
747 locations have been previously addressed. This was tested by fitting bias  
748 correction factor for U specifically, rather than calculating bias-correction  
749 factors for LMT and subtracting the LMT partial column from GOSAT XCO<sub>2</sub> to  
750 estimate U. The bias variability for U did not improve when bias correction  
751 factors were calculated directly for U. In Section 4.2, discrepancies between  
752 the XCO<sub>2</sub> calculated from the aircraft and TCCON XCO<sub>2</sub> are seen in locations  
753 where both measurements are co-located, so this does point towards the  
754 reason being the profile extension.

755

#### 756 **5.1.5 Predicted and actual error correlations**

757 One surprising finding is that LMT and U actual errors are less than the  
758 predicted errors whereas the actual XCO<sub>2</sub> errors are larger than predicted,  
759 even though all three errors are calculated from the same error covariance  
760 (see Eqs. 7-8). Equation 9c relates the errors in LMT, U, and XCO<sub>2</sub>. For  
761 land, the XCO<sub>2</sub> predicted error of 0.9 ppm is consistent with LMT predicted  
762 error of 4.6 ppm, U error of 1.8 ppm, and error correlation of -0.8. The  
763 XCO<sub>2</sub> actual error (1.7 ppm) is much *larger* than the predicted error whereas  
764 the LMT and U errors are *smaller* than predicted.

765

766 The discrepancy between the actual and predicted errors arises from the  
767 actual correlation of the LMT and U partial column errors. The predicted  
768 error correlation between LMT and U is -0.8. This means that values too low  
769 in LMT should be matched with values too high in U, such that the total  
770 column should have lower relative errors than either partial column  
771 separately. The actual error correlation of (LMT-aircraft) and (U-aircraft)  
772 average +0.6, meaning that when LMT is high, U also tends to be high, and



773 XCO<sub>2</sub> does not gain precision when combining LMT and U. So the finding is  
774 that the LMT-U error correlation must be changed from the predicted value  
775 of -0.8 to the measured value of +0.6. When this error correlation is  
776 changed and all error terms multiplied by approximately \*0.6, the predicted  
777 and actual errors of LMT, U, and XCO<sub>2</sub> are consistent. Over ocean, the error  
778 correlation is the same, but the multiplication factor is

779

780 The errors in Table 3 are the standard deviation with respect to validation  
781 data at one location. The persistent regional biases captured in the "GOSAT  
782 bias" standard deviation also reflect errors in the GOSAT measurement and  
783 should somehow be combined into the full error. These regional biases likely  
784 result from persistent interferent errors, such as due to aerosols, or an  
785 interaction between spectroscopic errors and local conditions. Some but not  
786 all of the bias, particularly for LMT land, can be attributed to co-location  
787 error (see bias ct\_ct (ppm) in Table 3). The correlation of the LMT and U  
788 location-dependent biases (using biases separated by location from Table  
789 B1) is also positive, 0.6, similar to the correlation of the individual errors in  
790 LMT and U, so this would not account for the discrepancy between the  
791 predicted correlation of -0.8 and actual correlation of 0.6 between the LMT  
792 and U errors. Another possible reason for the positive error correlation in  
793 LMT and U is that it is a consequence of the bias correction. The error  
794 correlation on the uncorrected data was found to be -0.8, which supports  
795 that the bias correction modifies the error correlation between U and LMT.

796

797 In summary, the single-sounding errors of GOSAT LMT and U over land  
798 (ocean), based on the ESRL aircraft comparison, are 3.4 and 1.3 ppm (1.5  
799 and 0.8 ppm) respectively, with a positive correlation of 0.6. This is  
800 consistent with the XCO<sub>2</sub> error of 1.8 (1.0) ppm for land (ocean), using Eq.  
801 9c. To find the error of averaged LMT and U, the single-sounding errors can  
802 be replaced by Eq 11, with a and b values given in Table 4, and the same  
803 LMT-U correlation of 0.6.

804

## 805 **5.2 Variability within the U.S.**

806 The CarbonTracker model identifies 19 eco-regions within North America  
807 ([http://www.esrl.noaa.gov/qmd/ccgg/carbontracker/CT2011\\_oj/documentati](http://www.esrl.noaa.gov/qmd/ccgg/carbontracker/CT2011_oj/documentati)  
808 [on\\_assim.html](http://www.esrl.noaa.gov/qmd/ccgg/carbontracker/CT2011_oj/documentati)). The ESRL aircraft stations can be broadly grouped into  
809 conifer forest: pfa, etl, esp, thd; grass/shrub: car, bne; crops: hil, wbj,  
810 sgp; forest/field: dnd, lef, nha, cma, sca; and mixed: tgc. The variability  
811 at these sites is a combination of the local activity at the site, latitude of the  
812 site, and transport into/out of the site.

813

814 Maps of GOSAT LMT, U, and XCO<sub>2</sub> along with aircraft, surface, tower, and  
815 TCCON observations for February and July are shown in Fig. 6. In February,  
816 the lower troposphere has already reached near peak values, whereas the U



817 partial column is continuing to increase through April. In July, there is a  
818 large gradient in the LMT, primarily west to east, but also north to south,  
819 seen also in the stations shown in Fig. 6. The LMT pattern agrees with  
820 aircraft and tower patterns, showing that GOSAT LMT is able to see  
821 variations in the summertime CO<sub>2</sub> depletion near the surface due to  
822 biospheric processes. The U partial column shows more discrepancies with  
823 aircraft than LMT which is in general agreement, and the same pattern of  
824 discrepancies are also seen for XCO<sub>2</sub> versus aircraft. At the two sites where  
825 aircraft and TCCON are jointly observed, SGP in Oklahoma and LEF in  
826 Wisconsin, XCO<sub>2</sub> agrees with TCCON rather than the aircraft. This indicates  
827 an issue with the extension of the aircraft profile from the top aircraft  
828 measurement (about 6 km) to the top of the atmosphere.

829  
830 Figure 7 shows the seasonal cycle at 5 sites arranged west-to-east (a-e) and  
831 north-to-south (f-j). The seasonal cycle amplitude in LMT increases  
832 traversing the region in both west-to-east and south-to-north directions.  
833 There is also a shift to later in the seasonal cycle minimum going either west  
834 to east and north to south. The seasonal cycle maximum is harder to  
835 quantify for the LMT. The LMT CO<sub>2</sub> rises and stays fairly flat from January to  
836 April, therefore the maximum can be influenced by small temporal variations  
837 in the data, in contrast to U or XCO<sub>2</sub> which rises steadily until April.

838

### 839 **5.3 Comparisons to remote ocean sites**

840 Remote surface sites are useful as comparisons to LMT as these locations  
841 are expected to be fairly well mixed in the boundary layer. These  
842 comparisons are not used for estimating errors or bias corrections because  
843 there could be a mismatch in airmass. Comparisons to surface sites are  
844 direct comparisons without the averaging kernel applied, as there is no  
845 profile information at these sites. The vertical co-location error is estimated  
846 by comparing CarbonTracker LMT versus CarbonTracker surface values in  
847 Tables 2 and 3. The GOSAT LMT a priori is significantly worse for these  
848 locations as compared to North America, and this allows the GOSAT product  
849 to show what is in the data versus the prior. In Table 4, the correlated error  
850 for surface sites is higher than for ocean aircraft comparisons (1.0 ppm vs.  
851 0.3 ppm, respectively), and the mean bias is also higher (0.7 ppm vs. 0.1  
852 ppm, respectively). Because of the GOSAT ocean coverage, there are  
853 typically only about 4 consecutive months for each station, but this is  
854 adequate to evaluate the performance. Figure 8 shows an average over all  
855 locations, and the 4 sites with the highest number of matches, arranged  
856 from north to south. Note the improvement of GOSAT (red) over the a priori  
857 (green) when comparing to the surface site measurements (pink).  
858 Unsurprisingly, the performance of XCO<sub>2</sub> (blue) shows that surface site  
859 observations are not suitable for XCO<sub>2</sub> validation. GOSAT LMT improves  
860 over the prior in terms of the overall bias, the bias variability, and the



861 standard deviation over the prior even without averaging; the error reduces  
862 further with averaging.

863

#### 864 **5.4 Source versus outflow in biomass burning with comparisons to** 865 **MOPITT CO**

866 The SH region is of particular interest for validation as the GOSAT prior is  
867 nearly spatially and vertically constant, varying primarily by month. GOSAT  
868 LMT and U partial columns are compared to MOPITT multispectral CO  
869 retrievals and MODIS fire counts for February, August, and September, 2010  
870 in Figs. 9 and 10. The GOSAT prior (left column in Figs 9-10) is nearly  
871 constant in the southern hemisphere. The scale needed to span the  
872 seasonal range is about 13 ppm, about half that needed for the variability in  
873 the U.S. The pattern seen in LMT matches MODIS fire count images, shown  
874 in the right column, and matches MOPITT near-surface CO shown in the  
875 middle column. Because of the different overpass time and the different  
876 coverage due to cloudiness between these satellites, an exact match should  
877 not be expected. Also, note that multi-spectral CO does not have surface  
878 sensitivity over ocean. In February, sub-Saharan Africa has fires and south-  
879 central Africa does not, whereas the situation is reversed in August. This  
880 pattern is seen in GOSAT LMT, MOPITT near-surface, and MODIS fire counts.

881

882 In the mid-troposphere, MOPITT CO shows enhancement in sub-Saharan  
883 Africa in February, central Africa in August, and outflow in October, and  
884 GOSAT retrieved U shows the same patterns as MOPITT. Interestingly, both  
885 MOPITT and GOSAT show no enhancement in South America in August,  
886 whereas the surface has very strong enhancements in both.

887

888 The LMT signal in the Amazon region is clearly visible by May (not shown),  
889 whereas the CO signal seen from MOPITT  
890 ([http://www.acom.ucar.edu/mopitt/MOPITT/data/plots6j/maps\\_mon.html](http://www.acom.ucar.edu/mopitt/MOPITT/data/plots6j/maps_mon.html))  
891 seems to ramp up starting in August. We look at the  $\Delta\text{CO}/\Delta\text{CO}_2$  emission  
892 ratio in May and August to check the enhancements seen in LMT relative to  
893 MOPITT in these two months has a similar ratio is seen both months. The  
894 enhancements and background values for surface CO and LMT CO<sub>2</sub> are  
895 shown in Table 5.

896

897 The emission ratio estimate is calculated by taking the ratio of MOPITT  
898 multispectral CO divided by GOSAT LMT, each with their background  
899 subtracted. The raw emission ratio (which does not consider the sensitivity)  
900 is 4.7% for May, 2010 and 5.8% for August, 2010, using the degrees of  
901 freedom (DOFs) > 0.3 data. If "all MOPITT" data is used, the raw emission  
902 ratio for May and August, 2010 is 2.2% and 2.3%, respectively. The ratio  
903 dropping to half makes sense because the average MOPITT DOFs drops by  
904 half between these two categories. Based on the relative DOFs between



905 MOPITT and GOSAT, the emission ratios are likely about 10%, however, the  
906 dropoff of the vertical sensitivity would also need to be taken into account.  
907 Without utilizing a model as a transfer function, the exact ratio cannot be  
908 estimated, due to the varying sensitivities with altitude and observation  
909 locations and times. The emission ratio seen by the MOPITT and GOSAT  
910 LMT products are consistent with those estimated from aircraft observations  
911 over tropical forests by Akagi et al. (2011, Table 1), which is 8.8%. The  
912 ratio is consistent (within 2%) between May and August, and the ratio is  
913 consistent with aircraft observations. If, instead, the emission ratio were  
914 calculated from column XCO<sub>2</sub> and CO, the free troposphere and stratospheric  
915 variations in CO and CO<sub>2</sub> would need be either zero or solely from locally  
916 influenced fires.

917

### 918 **5.5 Differences between LMT and U**

919 The difference between CO<sub>2</sub> in the free troposphere and boundary layer can  
920 be used to evaluate model transport. One previous finding is that surface  
921 assimilation estimates of northern minus southern hemisphere land flux are  
922 correlated with the difference between CO<sub>2</sub> at 4 km and 1 km in the  
923 assimilated model. When the vertical difference of CO<sub>2</sub> is larger than aircraft  
924 observations, models tend to predict too large northern hemisphere sinks  
925 and too large southern hemisphere sources (Stephens et al., 2007).  
926 Measurements CO<sub>2</sub> and 4 km and 1 km are performed only at a few sites  
927 worldwide, primarily in the U.S. Therefore, global measurements of the  
928 difference between CO<sub>2</sub> in the free troposphere and boundary layer are of  
929 great interest. In this section we calculate the errors for LMT-U compared to  
930 aircraft profiles and show this difference for GOSAT and CarbonTracker in  
931 the U.S. and the southern hemisphere in two different months.

932

933 The error estimate for LMT-U is calculated using Eq. 13. Note that a positive  
934 correlation in the errors for LMT and U results in a smaller error for the  
935 quantity (LMT - U).

936

$$937 \sigma_{(LMT-U)} = \sqrt{\sigma_{lmt}^2 + \sigma_u^2 - 2 * \sigma_{lmt}\sigma_u corr} \quad (13)$$

938

939 Table 5a-c give the bias, standard deviation, and error with averaging for  
940 LMT - U. In Table 5a, the GOSAT bias and bias variability of (LMT - U)  
941 improves over the prior for all cases. The bias variability of 0.3, 0.9 and 0.8  
942 ppm of (LMT - U) for HIPPO ocean, ESRL ocean, and ESRL land,  
943 respectively, is comparable to the LMT bias variability of 0.3, 1.0, and 1.0 for  
944 the same categories. In Table 5b, the 15-observation average standard  
945 deviation for GOSAT LMT-U is 0.6 (1.2) ppm for ocean (land), 0.2 ppm  
946 higher for ocean and 0.7 ppm lower for land than LMT. In Table 5c, the  
947 correlated error is 0.5 (0.9) ppm for ocean (land), which is 0.2 ppm higher  
948 for ocean and 0.8 ppm lower for land. The land standard deviation for LMT-



949 U is 2.3 ppm before subtracting off the 2.1 ppm co-location error. The  
950 difference between the land error for LMT and LMT-U is due to the estimated  
951 size of the co-location error.

952  
953 Figure 11 shows the seasonal cycle of LMT-U for 3 sites. The differences  
954 between GOSAT and aircraft values at the CAR site in Colorado and LEF in  
955 Wisconsin during the drawdown can be explained by co-location error. The  
956 dotted lines shows CarbonTracker matched to GOSAT (red dotted) or aircraft  
957 (pink dotted) locations/times. The difference between the red dotted and  
958 pink dotted lines estimate the co-location error. If GOSAT were corrected by  
959 this difference, the agreement with aircraft would be much better. The co-  
960 location bias and standard deviation are estimated in Tables 6a and 6b, and  
961 are large compared to the observed GOSAT errors. The error estimates for  
962 GOSAT are corrected by the co-location error.

963  
964 The predicted error for land in Table 6b is 2.7 ppm, whereas the actual error  
965 is 2.3 ppm. If LMT and U had zero correlation, the predicted error (using Eq.  
966 13) would be 3.6 ppm. This is another corroboration of the positive  
967 correlation between the LMT and U errors.

968  
969 Figure 12 shows LMT - U for February and July in the U.S. averaged over  
970 2010-2014 for February and 2009-2013 for July. Aircraft values for LMT - U  
971 are shown as squares. The aircraft patterns are captured by GOSAT, with  
972 discrepancies in July for CAR, SGP, and SCA due to co-location error (e.g.  
973 see CAR plot in Fig. 11). The CarbonTracker model captures the aircraft  
974 patterns very well. The two maps show differences in the southwestern U.S.  
975 in July, where there are no aircraft measurements. Figure 12c-d shows LMT  
976 - U for February and October in the southern hemisphere. The only aircraft  
977 site in this region is Rarotonga, where Fig. 11 shows good agreement for  
978 CarbonTracker and GOSAT. The patterns in the southern hemisphere show  
979 some differences between CarbonTracker and GOSAT. In February, GOSAT  
980 shows a high gradient in the eastern Pacific and northern South America not  
981 seen in CarbonTracker, and more negative gradient in central and southern  
982 Africa. In October large gradients are seen by GOSAT in South America and  
983 Africa with outflow into the Atlantic, with little seen in CarbonTracker.

984  
985 LMT-U is predominantly positive in this southern hemisphere region in  
986 October. Vertical transport from the northern hemisphere would  
987 predominantly show up in the U partial column, whereas flux from land or  
988 ocean would predominantly show up in the LMT partial column. An overall  
989 positive value for LMT - U could either suggest that the overall flux is  
990 positive in this month, or that transport from the northern hemisphere was  
991 negative, though the blank space in the Amazon due to cloudy conditions,  
992 where LMT-U is expected to be negative from plant uptake, creates



993 uncertainty both in this crude estimate and in the formal assimilated results  
994 from GOSAT data.

995

## 996 **6.0 Discussion and conclusions**

997 GOSAT near-infrared observations provide information to retrieve two partial  
998 columns, one from the surface to about 2.5 km (LMT\_XCO<sub>2</sub>), and the second  
999 above about 2.5 km (U\_XCO<sub>2</sub>). The LMT partial column is sensitive near the  
1000 surface, whereas the U partial column is sensitive to the free troposphere  
1001 and above; the two partial columns have distinct seasonal cycles, with peaks  
1002 and troughs earlier for the LMT partial column, and later for the U partial  
1003 column, as compared to XCO<sub>2</sub>. After bias correction, both partial columns  
1004 show agreement with aircraft, LMT shows agreement with remote surface  
1005 observations, and both show improvement over the GOSAT prior. Single  
1006 observations for land have observation errors of 3.4, 1.3, and 1.7 ppm for  
1007 LMT, U, and XCO<sub>2</sub>, respectively, and single observations for ocean have  
1008 observation errors of 1.5, 0.8, and 0.9 ppm for LMT, U, and XCO<sub>2</sub>,  
1009 respectively. These errors are significantly reduced with averaging, though  
1010 some systematic errors, generally below 1 ppm, remain. The co-location  
1011 errors from mismatch of GOSAT versus validation data, as quantified by  
1012 CarbonTracker, makes the errors on LMT challenging to validate. The value  
1013 of observing two partial columns can be seen in Fig. 8, where the GOSAT  
1014 LMT agrees with remote surface sites whereas neither the prior nor XCO<sub>2</sub>  
1015 agree with the surface site, and Figs. 9-10, where surface versus  
1016 tropospheric CO<sub>2</sub> are distinguished for source and outflow of African biomass  
1017 burning emissions in August and October. The observed LMT CO<sub>2</sub>  
1018 enhancements are consistent with MOPITT multispectral CO and emission  
1019 ratios in Akagi et al. (2011). The LMT-U difference, which can be used to  
1020 evaluate model transport error (e.g. Stephens et al., 2007), has also been  
1021 validated with monthly average error of 0.8 (1.4) ppm for ocean (land). The  
1022 new LMT partial column allows the local boundary air to be distinguished  
1023 from the free troposphere, captured in the U partial column, disentangling  
1024 local versus remotely influenced signals.

1025

1026

### 1027 **Funding Acknowledgements:**

1028 This research was funded by NASA and performed under BAER Institute's  
1029 ARC-CREST cooperative agreement.

1030

1031 The AJAX team recognizes the support and partnership of H211 L. L. C. and  
1032 the NASA Postdoctoral Program; funding for instrumentation and aircraft  
1033 integration is gratefully acknowledged from Ames Research Center Director's  
1034 funds.

1035





1036 CarbonTracker CT2015 results provided by NOAA ESRL, Boulder, Colorado,  
1037 USA from the website at <http://carbontracker.noaa.gov>.  
1038  
1039 Part of this work was carried out at the Jet Propulsion Laboratory, California  
1040 Institute of Technology, under a contract with NASA.  
1041  
1042 TCCON at Lamont and Park Falls are funded by NASA grants NNX14AI60G,  
1043 NNX11AG01G, NAG5-12247, NNG05-GD07G, and NASA Orbiting Carbon  
1044 Observatory Program, with the DOE ARM program providing technical  
1045 support in Lamont and Jeff Ayers providing technical support in Park Falls.  
1046  
1047

1048 **References**

1049

1050 Akagi, S. K., Yokelson, R. J., Wiedinmyer, C., Alvarado, M. J., Reid, J. S.,  
1051 Karl, T., Crounse, J. D., and Wennberg, P. O.: Emission factors for open and  
1052 domestic biomass burning for use in atmospheric models, *Atmos. Chem.*  
1053 *Phys.*, 11, 4039-4072, doi:10.5194/acp-11-4039-2011, 2011.

1054 Baker, D. F., Law, R. M., Gurney, K. R., Rayner, P., Peylin, P., Denning, A.  
1055 S., Bousquet, P., Bruhwiler, L., Chen, Y. H., Ciais, P., Fung, I. Y.,  
1056 Heimann, M., John, J., Maki, T., Maksyutov, S., Masarie, K., Prather,  
1057 M., Pak, B., Taguchi, S., and Zhu, Z.: TransCom 3 inversion  
1058 intercomparison: Impact of trans-port model errors on the interannual  
1059 variability of regional CO<sub>2</sub> fluxes, 1988-2003, *Global Biogeochem. Cy.*, 20,  
1060 GB1002, doi:10.1029/2004GB002439, 2006.

1061 Bowman, K. W., Rodgers, C. D., Kulawik, S. S., Worden, J., Sarkissian, E.,  
1062 Osterman, G., Steck, T., Lou, M., Eldering, A., Shephard, M., Worden, H.,  
1063 Lampel, M., Clough, S., Brown, P., Rinsland, C., Gunson, M., and Beer, R.:  
1064 Tropospheric emission spectrometer: Retrieval method and error analysis,  
1065 *IEEE T. Geosci. Remote*, 44(5), 1297–1307, 2006.

1066 Chevallier, F., Ciais, P., Conway, T. J., Aalto, T., Anderson, B. E., Bousquet,  
1067 P., Brunke, E. G., Ciattaglia, L., Esaki, Y., Frohlich, M., Gomez, A. J., Gomez-  
1068 Pelaez, A. J., Haszpra, L., Krummel, P., Langenfelds, R., Leuenberger, M.,  
1069 Machida, T., Maignan, F., Matsueda, H., Morgui, J. A., Mukai, H., Nakazawa,  
1070 T., Peylin, P., Ramonet, M., Rivier, L., Sawa, Y., Schmidt, M., Steele, P.,  
1071 Vay, S. A., Vermeulen, A. T., Wofsy, S., and Worthy, D.: CO<sub>2</sub> surface fluxes  
1072 at grid point scale estimated from a global 21-year reanalysis of atmospheric  
1073 measurements, *J. Geophys. Res.*, 115, D21307,  
1074 doi:10.1029/2010JD013887, 2010.

1075 Chevallier, F., Palmer, P. I., Feng, L., Boesch, H., O'Dell, C. W., and  
1076 Bousquet, P.: Toward robust and consistent regional CO<sub>2</sub> flux estimates  
1077 from in situ and spaceborne measurements of atmospheric CO<sub>2</sub>, *Geophys.*  
1078 *Res. Lett.*, 41, 1065-1070, doi:10.1002/2013GL058772, 2014.

1079 Connor, B. J., Sherlock, V., Toon, G., Wunch, D., and Wennberg, P.: GFIT2:  
1080 an experimental algorithm for vertical profile retrieval from near IR spectra,  
1081 *Atmos. Meas. Tech. Discuss.*, 8, 12263-12295, doi:10.5194/amtd-8-12263-  
1082 2015, 2015.

1083 Connor, B. J., H. Boesch, G. Toon, B. Sen, C. Miller, and D. Crisp, Orbiting  
1084 Carbon Observatory: Inverse method and prospective error analysis, *J.*  
1085 *Geophys. Res.*, 113, D05305, doi:10.1029/2006JD008336, 2008.

1086 Conway, T. J., Tans, P. P., Waterman, L. S., Thoning, K. W., Kitzis, D. R.,  
1087 Masarie, K. A., and Zhang, N.: Evidence for interannual variability of the



- 1088 carbon cycle from the NOAA/CMDL global air sampling network, *J. Geophys.*  
1089 *Res.*, 99, 22831-22855, 1994.
- 1090 Cooperative Global Atmospheric Data Integration Project, 2013, updated  
1091 annually. Multi-laboratory compilation of atmospheric carbon dioxide data for  
1092 the period 2000-2012 (obspack\_co2\_1\_PROTOTYPE\_v1.0.4b\_2014-02-13).  
1093 Compiled by NOAA Global Monitoring Division: Boulder, Colorado, U.S.A.  
1094 Data product accessed at <http://dx.doi.org/10.3334/OBSPACK/1001>.
- 1095 Crisp, D., B. M. Fisher, C. W. O'Dell, C. Frankenberg, R. Basilio, H. Bösch, L.  
1096 R. Brown, R. Castano, B. J. Connor, N. M. Deutscher, A. Eldering, D. Griffith,  
1097 M. Gunson, A. Kuze, L. Mandrake, J. McDuffie, J. Messerschmidt, C. E. Miller,  
1098 I. Morino, V. Natraj, J. Notholt, D. M. O'Brien, F. Oyafuso, I. Polonsky, J.  
1099 Robinson, R. Salawitch, V. Sherlock, M. Smyth, H. Suto, T. E. Taylor, D. R.  
1100 Thompson, P. O. Wennberg, D. Wunch, and Y. L. Yung, The ACOS CO<sub>2</sub>  
1101 retrieval algorithm - Part II: Global XCO<sub>2</sub> data characterization, *Atmospheric*  
1102 *Measurement Techniques*, 5(4), 687-707, doi:10.5194/amt-5-687-2012,  
1103 2012.
- 1104 Davies, D., Kumar, S., and Desclotres, J., Global fire monitoring using  
1105 MODIS near-real-time satellite data. *GIM International*, 18(4):41-43, 2004.
- 1106 Deeter, M. N., et al., Operational carbon monoxide retrieval algorithm and  
1107 selected results for the MOPITT instrument, *J. Geophys. Res.*, 108(D14),  
1108 4399, doi:10.1029/2002JD003186, 2003.
- 1109 Deeter, M. N., Martinez-Alonso, S., Edwards, D. P., Emmons, L. K., Gille, J.  
1110 C., Worden, H. M., Sweeney, C., Pittman, J. V., Daube, B. C., and Wofsy, S.  
1111 C.: The MOPITT Version 6 product: algorithm enhancements and validation,  
1112 *Atmos. Meas. Tech.*, 7(11), 3623-3632, 2014.
- 1113 Deng, F., Jones, D. B. A., Walker, T. W., Keller, M., Bowman, K. W., Henze,  
1114 D. K., Nassar, R., Kort, E. A., Wofsy, S. C., Walker, K. A., Bourassa, A. E.,  
1115 and Degenstein, D. A.: Sensitivity analysis of the potential impact of  
1116 discrepancies in stratosphere-troposphere exchange on inferred sources and  
1117 sinks of CO<sub>2</sub>, *Atmos. Chem. Phys.*, 15, 11773-11788, doi:10.5194/acp-15-  
1118 11773-2015, 2015.
- 1119 Denning, A. S., Collatz, G. J., Zhang, C., Randall, D. A., Berry, J. A.,  
1120 Sellers, P. J., Colello, G. D., and Dazlich, D. A.: Simulations of terrestrial  
1121 carbon metabolism and atmospheric CO<sub>2</sub> in a general circulation model. Part  
1122 2: simulated CO<sub>2</sub> concentrations, *Tellus*, 48B, 543-567, 1996.
- 1123 Dohe, S., Measurements of atmospheric CO<sub>2</sub> columns using ground-based  
1124 FTIR spectra, Doctor of Science dissertation, Karlsruhe Institute for  
1125 Technology, Karlsruhe, Germany, 2013.
- 1126 Feng, L., Palmer, P. I., Parker, R. J., Deutscher, N. M., Feist, D. G., Kivi, R.,  
1127 Morino, I., and Sussmann, R.: Estimates of European uptake of CO<sub>2</sub> inferred



- 1128 from GOSAT X-CO<sub>2</sub> retrievals: sensitivity to measurement bias inside and  
1129 outside Europe, *Atmospheric Chemistry And Physics*, 16, 1289-1302,  
1130 doi:10.5194/acp-16-1289-2016, 2016.
- 1131 Giglio, L., J. Descloitres, C. O. Justice, and Y. J. Kaufman, An enhanced  
1132 contextual fire detection algorithm for MODIS. *Remote Sensing of*  
1133 *Environment*, 87:273-282, 2003.
- 1134 Guerlet, S., Butz, A., Schepers, D., Basu, S., Hasekamp, O. P., Kuze, A.,  
1135 Yokota, T., Blavier, J.-F., Deutscher, N. M., Griffith, D. W. T., Hase, F., Kyro,  
1136 E., Morino, I., Sherlock, V., Sussmann, R., Galli, A., Aben, I., *J. Geophys.*  
1137 *Res. Atmos.*, 118, 4887-4905, doi:10.1002/jgrd.50332, 2013.
- 1138 Gurney, K. R., Law, R. M., Denning, A. S., Rayner, P. J., Baker, D.,  
1139 Bousquet, P., Bruhwiler, L., Chen, Y.-H., Ciais, P., Fan, S., Fung, I. Y., Gloor,  
1140 M., Heimann, M., Higuchi, K., John, J., Maki, T., Maksyutov, S., Masarie, K.,  
1141 Peylin, P., Prather, M., Pak, B. C., Randerson, J., Sarmiento, J., Taguchi, S.,  
1142 Takahashi, T., and Yuen, C.-W.: Towards robust regional estimates of CO<sub>2</sub>  
1143 sources and sinks using atmospheric transport models, *Nature*, 415, 626-  
1144 630, 2002.
- 1145 Hamill, P., L. Iraci, E. Yates, W. Gore, T. P. Bui, T. Tanaka, and M.  
1146 Loewenstein (2016), A new instrumented airborne platform for atmospheric  
1147 research, *Bulletin of the American Meteorological Society*. vol. 97, no. 3,  
1148 doi:10.1175/BAMS-D-14-00241.1.
- 1149 Houweling, S., Baker, D., Basu, S., Boesch, H., Butz, A., Chevallier, F.,  
1150 Deng, F., Dlugokencky, E. J., Feng, L., Ganshin, A., Hasekamp, O., Jones,  
1151 D., Maksyutov, S., Marsha, J., Oda, T., O'Dell, C. W., Oshchepkov, S.,  
1152 Palmer, P. I., Peylin, P., Poussi, Z., Reum, F., Takagi, H., Yoshida, Y., and  
1153 Zhuravlev, R.: An intercomparison of inverse models for estimating sources  
1154 and sinks of CO<sub>2</sub> using GOSAT measurements, *J. Geophys. Res. Atmos.*,  
1155 120, 5253-5266, 2015.
- 1156 Inoue, M., Morino, I., Uchino, O., Miyamoto, Y., Yoshida, Y., Yokota,  
1157 T., Machida, T., Sawa, Y., Matsueda, H., Sweeney, C., Tans, P. P., Andrews,  
1158 A. E., Biraud, S. C., Tanaka, T., Kawakami, S., and Patra, P. K.:  
1159 Validation of XCO<sub>2</sub> derived from SWIR spectra of GOSAT TANSO-FTS with  
1160 aircraft measurement data, *Atmos. Chem. Phys.*, 13, 9771-9788, doi:  
1161 10.5194/acp-13-9771-2013, 2013.
- 1162 Kuai L., Wunch, D., Shia, R.-L., Connor, B., Miller, C., and Yung, Y.:  
1163 Vertically constrained CO<sub>2</sub> retrievals from TCCON measurements, *J. Quant.*  
1164 *Spectrosc. Ra.*, 113, 1753-1761, 2012.
- 1165 Kulawik, S. S., Osterman, G., Jones, D. B. A., and Bowman, K.W.,  
1166 Calculation of altitude-dependent Tikhonov constraints for TES nadir  
1167 retrievals, *IEEE T. Geosci. Remote*, 44(5), 1334-1342, 2006.



- 1168 Kulawik, S., Wunch, D., O'Dell, C., Frankenberg, C., Reuter, M., Oda, T.,  
1169 Chevallier, F., Sherlock, V., Buchwitz, M., Osterman, G., Miller, C. E.,  
1170 Wennberg, P. O., Griffith, D., Morino, I., Dubey, M. K., Deutscher, N. M.,  
1171 Notholt, J., Hase, F., Warneke, T., Sussmann, R., Robinson, J., Strong, K.,  
1172 Schneider, M., De Mazière, M., Shiomi, K., Feist, D. G., Iraci, L. T., and Wolf,  
1173 J.: Consistent evaluation of ACOS-GOSAT, BESD-SCIAMACHY,  
1174 CarbonTracker, and MACC through comparisons to TCCON, Atmos. Meas.  
1175 Tech., 9, 683-709, doi:10.5194/amt-9-683-2016, 2016.
- 1176 Kuze, A., Suto, H., Shiomi, K., Kawakami, S., Tanaka, M., Ueda, Y.,  
1177 Deguchi, A., Yoshida, J., Yamamoto, Y., Kataoka, F., Taylor, T. E., and Buijs,  
1178 H. L.: Update on GOSAT TANSO-FTS performance, operations, and data  
1179 products after more than 6 years in space, Atmos. Meas. Tech., 9, 2445-  
1180 2461, doi:10.5194/amt-9-2445-2016, 2016.
- 1181 Lauvaux, T. and Davis, K. J.: Planetary boundary layer errors in mesoscale  
1182 inversions of column-integrated CO<sub>2</sub> measurements, J. Geophys. Res.-  
1183 Atmos., 119, 490-508, doi:10.1002/2013jd020175, 2014.
- 1184 Liu, J., I. Fung, E. Kalnay, and J. S. Kang, CO transport uncertainties from  
1185 the uncertainties in meteorological fields, Geophys. Res. Lett., 38, L12808,  
1186 doi:10.1029/2011GL047213, 2011.
- 1187 Liu, J., Bowman, K. W., and Henze, D. K.: Source-receptor relationships of  
1188 column-average CO<sub>2</sub> and implications for the impact of observations on flux  
1189 inversions, J. Geophys. Res. Atmos., 120, 5214-5236, 2015.
- 1190 Miller, C. E., D. Crisp, P. L. DeCola, S. C. Olsen, J. T. Randerson, A. M.  
1191 Michalak, A. Alkhaled, P. Rayner, D. J. Jacob, P. Suntharalingam, D. B. A.  
1192 Jones, A. S. Denning, M. E. Nicholls, S. C. Doney, S. Pawson, H. Boesch, B. J.  
1193 Connor, I. Y. Fung, D. O'Brien, R. J. Salawitch, S. P. Sander, B. Sen, P.  
1194 Tans, G. C. Toon, P. O. Wennberg, S. C. Wofsy, Y. L. Yung, and R. M. Law,  
1195 Precision requirements for space-based XCO<sub>2</sub> data, J. Geophys. Res., 112,  
1196 D10314, doi:10.1029/2006JD007659, 2007.
- 1197 Nehr Korn, T., J. Eluszkiewicz, S. C. Wofsy, J. C. Lin, C. Gerbig, M. Longo and  
1198 S. Freitas, Coupled Weather Research and Forecasting-Stochastic-Time-  
1199 Inverted Lagrangian Transport Model, Meteorol. Atmos. Phys., 107: 51-64,  
1200 2010.
- 1201 O'Brien, D. M., and P. J. Rayner, Global observations of the carbon budget,  
1202 2, CO<sub>2</sub> concentrations from differential absorption of reflected sunlight in the  
1203 1.61 μm band of CO<sub>2</sub>, J. Geophys. Res., 107(D18), 4354,  
1204 doi:10.1029/2001JD000617, 2002.
- 1205 Peters, Wouter, Jacobson, Andrew R., Sweeney, Colm, Andrews, Arlyn E.,  
1206 Conway, Thomas J., Masarie, Kenneth, Miller, John B., Bruhwiler, Lori M. P.,  
1207 Petron, Gabrielle, Hirsch, Adam I., Worthy, Douglas E. J., van der Werf,  
1208 Guido R., Randerson, James T., Wennberg, Paul O., Krol, Maarten C., and



- 1209 Tans, Pieter P.: An atmospheric perspective on North American carbon  
1210 dioxide exchange: CarbonTracker, Proceedings Of The National Academy Of  
1211 Sciences Of The United States Of, 104, 18925-18930,  
1212 doi:10.1073/pnas.0708986104, 2007.
- 1213 Prather, M. J.; Zhua, X; Strahan, SE; Steenrod, SD; Rodriguez, JM,  
1214 Quantifying errors in trace species transport modeling. Proceedings of the  
1215 National Academy of Sciences of the United States of America 105(50),  
1216 19617-19621. DOI: 10.1073/pnas.0806541106, Dec 16, 2008
- 1217 Rayner, P. J., and O'Brien, D. M., The utility of remotely sensed CO<sub>2</sub>  
1218 concentration data in surface source inversions (vol 28, pg 175, 2001),  
1219 Geophys. Res. Lett., 28, 2429-2429, doi:10.1029/2001GL013115, 2001.
- 1220 Rodgers, C. D. In: Inverse methods for atmospheric sounding: theory and  
1221 practice. London. WorldScientific, 2000.
- 1222 Steck, T. and von Clarmann, T., Constrained profile retrieval applied to the  
1223 observation mode of the Michelson Interferometer for Passive Atmospheric  
1224 Sounding, Appl. Opt., 40, 3559-3571, 2001.
- 1225 Stephens, B. B., Gurney, K. R., Tans, P. P., Sweeney, C., Peters, W.,  
1226 Bruhwiler, L., Ciais, P., Ramonet, M., Bousquet, P., Nakazawa, T., Aoki, S.,  
1227 Machida, T., Inoue, G., Vinnichenko, N., Lloyd, J., Jordan, A., Heimann, M.,  
1228 Shibistova, O., Langenfelds, R. L., Steele, L. P., Francey, R. J., and Denning,  
1229 A. S.: Weak northern and strong tropical land carbon uptake from vertical  
1230 profiles of atmospheric CO<sub>2</sub>, Science, 2007 Jun 22;316(5832), 1732 - 5,  
1231 2007.
- 1232 Tanaka, T., E. Yates, L. Iraci, M. Johnson, W. Gore, J. Tadic, M. Loewenstein,  
1233 A. Kuze, C. Frankenberg, A. Butz, and Y. Yoshida (2015), Two years  
1234 comparison of airborne measurements of CO<sub>2</sub> and CH<sub>4</sub> with GOSAT at  
1235 Railroad Valley, Nevada, in press at IEEE Transactions on Geoscience and  
1236 Remote Sensing. doi: 10.1109/TGRS.2016.2539973.
- 1237 Tikhonov, A.: On the solution of incorrectly stated problems and a method of  
1238 regularization, Dokl. Acad. Nauk SSSR, vol. 151, pp. 501 - 504, 1963.
- 1239 Twomey, S.: On the Numerical Solution of Fredholm Integral Equations of  
1240 the First Kind by the Inversion of the Linear System Produced by  
1241 Quadrature, Journal of the Association for Computing Machinery, 1701. 10  
1242 NO. 1, pp. 97 - 101, 1963.
- 1243 von Clarmann, T., Glatthor, N., Grabowski, U., Hopfner, M., Kellmann, S.,  
1244 Kiefer, M., Linden, A., Mengistu Tsidu, G., Milz, M., Steck, T., Stiller,  
1245 G. P., Wang, D. Y., Fischer, H., Funke, B., Gil-Lopez, S., and Lopez-  
1246 Puertas, M.: Retrieval of temperature and tangent altitude pointing from  
1247 limb emission spectra recorded from space by the Michelson Interferometer



- 1248 for Passive Atmospheric Sounding (MIPAS), *J. Geophys. Res.*, 108, 4736,  
1249 doi:10.1029/2003JD003602, 2003.
- 1250 Wennberg, P. O., C. Roehl, D. Wunch, G. C. Toon, J.-F. Blavier, R.  
1251 Washenfelder, G. Keppel-Aleks, N. Allen, J. Ayers. 2014. TCCON data from  
1252 Park Falls, Wisconsin, USA, Release GGG2014R0. TCCON data archive,  
1253 hosted by the Carbon Dioxide Information Analysis Center, Oak Ridge  
1254 National Laboratory, Oak Ridge, Tennessee, U.S.A.  
1255 <http://dx.doi.org/10.14291/tcon.ggg2014.parkfalls01.R0/1149161>
- 1256 Wennberg, P. O. Wunch, D. Roehl, C., Blavier, J.-F., Toon, G. C., Allen, N.,  
1257 Dowell, P., Teske, K., Martin, C., and Martin., J., TCCON data from Lamont,  
1258 Oklahoma, USA, Release GGG2014R0. TCCON data archive, hosted by the  
1259 Carbon Dioxide Information Analysis Center, Oak Ridge National Laboratory,  
1260 Oak Ridge, Tennessee, U.S.A.  
1261 <http://dx.doi.org/10.14291/tcon.ggg2014.lamont01.R0/1149159>
- 1262 Wofsy, S. C., Daube, B. C., Jimenez, R., Kort, E., Pittman, J. V., Park, S.,  
1263 Commane, R., Xiang, B., Santoni, G., Jacob, D., Fisher, J., Pickett-Heaps, C.,  
1264 Wang, H., Wecht, K., Wang, Q.-Q., Stephens, B. B., Shertz, S., Watt, A. S.,  
1265 Romashkin, P., Campos, T., Haggerty, J., Cooper, W. A., Rogers, D., Beaton,  
1266 S., Hendershot, R., Elkins, J. W., Fahey, D. W., Gao, R. S., Moore, F.,  
1267 Montzka, S. A., Schwarz, J. P., Perring, A. E., Hurst, D., Miller, B. R.,  
1268 Sweeney, C., Oltmans, S., Nance, D., Hintsa, E., Dutton, G., Watts, L. A.,  
1269 Spackman, J. R., Rosenlof, K. H., Ray, E. A., Hall, B., Zondlo, M. A., Diao,  
1270 M., Keeling, R., Bent, J., Atlas, E. L., Lueb, R., and Mahoney, M. J.: HIPPO  
1271 Merged 10-second Meteorology, Atmospheric Chemistry, Aerosol Data  
1272 (R\_20121129). Carbon Dioxide Information Analysis Center, Oak Ridge  
1273 National Laboratory, Oak Ridge, Tennessee, USA,  
1274 doi:10.3334/CDIAC/hippo\_010, 2012.
- 1275 Worden, H. M., Deeter, M. N., Edwards, D. P., Gille, J. C., Drummond, J. R.,  
1276 and N?d?lec, P.: Observations of near-surface carbon monoxide from space  
1277 using MOPITT multispectral retrievals, *Journal Of Geophysical Research*  
1278 (*Atmospheres*), 115(d14), 1831-18314, 2010.
- 1279 Worden, J., Kulawik, S. S., Shephard, M. W., Clough, S. A., Worden, H.,  
1280 Bowman, K. and Goldman, A.. Predicted errors of tropospheric emission  
1281 spectrometer nadir retrievals from spectral window selection, *Journal of*  
1282 *Geophysical Research-Atmospheres*, 109, (D9), 2004.
- 1283 Wunch, D., Toon, G.C., Blavier, J.-F.L., Washenfelder, R.A., Notholt, J.,  
1284 Connor, B.J., Griffith, D.W.T., Sherlock, V., Wennberg, P.O.: The Total  
1285 Carbon Column Observing Network. *Phil. Trans. R. Soc. A*, 369,  
1286 doi:10.1098/rsta.2010.0240, 2011a.
- 1287 Wunch, D., Wennberg, P. O., Toon, G. C., Connor, B. J., Fisher, B.,  
1288 Osterman, G. B., Frankenberg, C., Mandrake, L., O'Dell, C., Ahonen, P., and



- 1289 et al.: A method for evaluating bias in global measurements of CO<sub>2</sub> total  
1290 columns from space, *Atmospheric Chemistry and Physics*, 11, 12 317-12  
1291 337, doi:10.5194/acp-11-12317-2011, URL <http://dx.doi.org/10.5194/acp->  
1292 11-12317-2011, 2011b.
- 1293 Yokota, T., Yoshida, Y., Eguchi, N., Ota, Y., Tanaka, T., Watanabe, H., and  
1294 Maksyutov, S.: Global Concentrations of CO<sub>2</sub> and CH<sub>4</sub> Retrieved from  
1295 GOSAT: First Preliminary Results, *Sola*, 5, 160-163, 2009.





## 1296 **Appendix A. Bias Correction**

1297

1298 The ACOS-GOSAT XCO<sub>2</sub> product undergoes bias correction (Wunch et al.,  
1299 2011) which significantly improves the errors (Kulawik, 2016). We apply  
1300 this same technique to correct the LMT product. Following the LMT  
1301 correction, U is corrected by subtracting the LMT partial column from ACOS-  
1302 GOSAT corrected XCO<sub>2</sub>, thus maintaining consistency between the [LMT,U]  
1303 partial columns and the total XCO<sub>2</sub> column after bias-correction.

1304

1305 To determine the LMT bias correction, GOSAT and aircraft data are matched  
1306 using dynamic coincidence criteria (Wunch, 2011), and the difference  
1307 between GOSAT LMT and aircraft LMT is calculated for all pairs versus each  
1308 potential parameter. In order to identify the critical bias-predicting  
1309 parameters, for those cases for which this difference has a clear slope, a  
1310 bias correction is applied iteratively, where the strongest parameter  
1311 dependence is corrected before the next parameters are tested. At the end  
1312 all parameters are fit simultaneously. Filters are applied to flag the data as  
1313 bad when the bias is significant even after correction. The parameters  
1314 considered for bias correction are: delta\_grad\_co2, albedo\_1, albedo\_2,  
1315 albedo\_3, albedo\_slope\_1, albedo\_slope\_2, albedo\_slope\_3, aod\_dust,  
1316 aod\_ice, aod\_total, b1offset, ice\_height, surfacePressure\_xa,  
1317 surfacePressureDiff, co2\_ratio, dp\_cld, h2o\_ratio, s32, xco2\_error, LMT\_dofs  
1318 (degrees of freedom for LMT partial column), U\_dofs (degrees of freedom for  
1319 U partial column), xco2\_dofs, asza, lza, and delta\_grad\_co2\_prime. These  
1320 parameters are described in the ACOS-GOSAT v3.5 user's guide with the  
1321 exception of delta\_grad\_co2\_prime which is defined as delta\_grad\_co2 with  
1322 the value set to 50 when it is greater than 50 for land, and the value set to -  
1323 10 when it is greater than -10 for ocean. Two figures of merit were  
1324 considered for the cutoffs and bias fits, (1) bias variability by location and  
1325 season and (2) the single-observation standard deviation. The former is the  
1326 standard deviation of the biases calculated in 4 seasons and for each  
1327 location/campaign. For both of these figures of merit, smaller is better.

1328

1329 By far the strongest bias is related to delta\_grad\_CO2. This parameter is  
1330 the difference between the retrieved CO<sub>2</sub> and a priori dry-air molefraction  
1331 between the surface and vertical level 13 (approximately 630 hPa for  
1332 soundings near sea level), and represents the slope of the retrieved CO<sub>2</sub>  
1333 profile in the troposphere. The resulting coefficient for this term is 0.396 for  
1334 ocean and 0.310 for land soundings. This indicates that, for ocean,  
1335 approximately 40% of the CO<sub>2</sub> attributed to the surface should be moved  
1336 from LMT to U, indicating that possibly (a) the troposphere is constrained  
1337 too much relative to the surface, (b) an issue with spectroscopy, or (c) some  
1338 other retrieval artefact. As the bias correction for simulated OCO-2 data is  
1339 very similar factor (Kulawik, unpublished result), with simulations run with



1340 no spectroscopic error, it is likely a consequence of the constraint, or some  
1341 other aspect of the retrieval.

1342

1343 The filtering cutoffs and bias terms are shown in Table A1. The errors  
1344 calculated by the bootstrap method (Rubin, 1981). The effects of the cutoffs  
1345 and bias corrections from Table A1 on biases and standard deviations is  
1346 shown in Table A2.

1347

1348 The overall land bias is not zero because the land bias constant correction  
1349 undergoes a final step to harmonize land and ocean observations by  
1350 matching GOSAT values for pairs of close land and ocean observations. The  
1351 results for different matching criteria are: 1 degree and 1 hour (25 matches,  
1352 bias -0.54 ppm in LMT and -0.96 ppm in XCO<sub>2</sub>), 2 degrees and 24 hours  
1353 (295 matches, 0.17 ppm in LMT and -0.61 ppm in XCO<sub>2</sub>), 4 degrees and 48  
1354 hours (4095 matches, 1.17 ppm in LMT and -0.09 ppm in XCO<sub>2</sub>), and using  
1355 dynamic coincidence criteria (422,542 matches, 0.29 ppm in LMT, -0.42 in  
1356 XCO<sub>2</sub>). Using the assumption that there is no bias in XCO<sub>2</sub>, the 4 degree, 48  
1357 hours result is used, and 1.17 ppm is added to the LMT constant bias for  
1358 land. This constant bias is subtracted from LMT, then the LMT partial  
1359 column is subtracted from XCO<sub>2</sub> to generate the corrected U partial column.

1360

1361 As seen from Tables A3a and A3b, all bias corrections are superior to the  
1362 uncorrected dataset, and all correction tests perform similarly in the bias  
1363 standard deviation and mean standard deviation, but with variability in the  
1364 overall bias, depending on the development set that is used. The overall  
1365 bias has some uncertainty on the order of 0.5 ppm.

1366

1367 Another potential error source that is quantified is the effect of different  
1368 profile extension schemes above aircraft observations. The ESRL aircraft  
1369 measurements go up to 5-8 km above ground, and the HIPPO observations  
1370 go up to 9-13 km above ground. 4 different profile extension methods are  
1371 tried above the aircraft: using (1) the GOSAT a priori profile, (2) extending  
1372 the top aircraft measurement to the tropopause with the GOSAT prior above  
1373 this, (3) the CT2015 model, and (4) extending the top aircraft measurement  
1374 to the tropopause with the CT2015 model above this. Table A4 shows the  
1375 land and ocean characteristics with each of the profile extension type. The  
1376 main effect is on the overall bias (up to 0.3 ppm) in the comparisons. One  
1377 issue is likely in the top 4 levels, from which a difference between a priori  
1378 and the true profile would propagate as a bias.

1379

1380 There were two ways that the developed bias correction was insulated from  
1381 the validation: (1) the bias correction uses dynamic coincidence criteria  
1382 (Wunch, 2011), whereas the comparisons to validation data use geometric  
1383 coincidence criteria ( $\pm 5$  degrees latitude and longitude, and  $\pm 1$  week). The



1384 overlap between these two sets is about 50%. (2) remote ocean surface  
1385 sites were not used to develop the bias correction. These locations are  
1386 expected to have good mixing between the surface and 2.5 km, but since we  
1387 do not have profiles at these locations, these observations are not used for  
1388 direct validation. These comparisons between GOSAT and remote surface  
1389 sites show excellent improvement over the GOSAT prior. (3) No data over  
1390 the southern hemisphere biomass burning is used in the bias correction, and  
1391 GOSAT compares very well to MOPITT in this region.

1392  
1393 The mean and standard deviation of the bias correction is  $-11.4 \pm 7.6$ ,  
1394  $2.7 \pm 2.7$  ppm for LMT and U land, respectively and  $-1.0 \pm 3.1$  ppm,  $-1.7 \pm 0.9$   
1395 ppm for LMT and U ocean, respectively. The mean and standard deviations  
1396 of the bias correction for XCO<sub>2</sub> are:  $-0.6 \pm 1.0$  ppm for land and  $-0.6 \pm 0.6$  for  
1397 ocean. The bias corrections are larger for the partial columns than for XCO<sub>2</sub>;  
1398 the size and variability of the bias correction is an indication of its  
1399 importance.

1400

1401

1402



1403 **Appendix B. Detailed comparisons by site and campaign**

1404

1405 In addition to the averaged results provided previously, Table B1 below  
1406 breaks down the validation results for each individual station. This table  
1407 could be useful for diagnosing outliers in the comparisons, looking at  
1408 correlations of site-to-site biases or standard deviations in LMT and U.

1409

1410



1411 Table 1

1412 Predicted errors and degrees of freedom for LMT and U. As seen in Table 2,

1413 the predicted errors are much larger than the actual errors.

	land	ocean
LMT error (ppm)	4.3 ppm	4.4 ppm
U error (ppm)	1.7 ppm	1.7 ppm
U,LMT pred. error correlation	-0.72	-0.78
LMT DOFs	0.86	0.86
U DOFs	0.84	0.83

1414

1415 Table 2. Biases versus aircraft. The top entries are the co-location biases.

1416 The second row is the mean and variability of the true state. The 3<sup>rd</sup> row are

1417 the prior bias, and the fourth set are the GOSAT bias (prior and GOSAT bias

1418 have co-location bias subtracted). All data is first averaged by location or

1419 campaign. The  $\pm$  represents the variability of the bias by location or

1420 campaign, a key metric in the data quality.

Type		Ocean surface (ppm)	HIPPO Ocean (ppm)	ESRL Ocean (ppm)	ESRL Land (ppm)	AJAX Land (ppm)
CT_CT bias (estimate of co-location bias)	LMT	-0.3 $\pm$ 0.3	-0.3 $\pm$ 0.2	-0.3 $\pm$ 0.4	-0.6 $\pm$ 0.7	-0.6
	U	-0.3 $\pm$ 0.8	0.1 $\pm$ 0.1	-0.1 $\pm$ 0.1	0.0 $\pm$ 0.2	0.0
	XCO <sub>2</sub>		0.0 $\pm$ 0.1	-0.1 $\pm$ 0.1	-0.1 $\pm$ 0.3	-0.1
true mean by site/campaign	LMT	391.3 $\pm$ 1.6	392.2 $\pm$ 1.6	391.7 $\pm$ 1.1	392.2 $\pm$ 3.1	393.6
	U		391.1 $\pm$ 1.2	391.3 $\pm$ 1.6	391.2 $\pm$ 0.6	392.2
	XCO <sub>2</sub>		391.4 $\pm$ 1.3	391.4 $\pm$ 1.5	391.5 $\pm$ 1.1	392.4
prior bias	LMT	-0.8 $\pm$ 1.5	0.1 $\pm$ 2.4	-1.5 $\pm$ 4.5	-0.4 $\pm$ 1.2	-1.4
	U		1.2 $\pm$ 0.1	-1.2 $\pm$ 1.6	0.6 $\pm$ 0.6	0.4
	XCO <sub>2</sub>		0.9 $\pm$ 1.4	0.4 $\pm$ 2.3	-0.2 $\pm$ 0.6	-0.1
GOSAT bias	LMT	1.1 $\pm$ 1.1	0.1 $\pm$ 0.3	0.3 $\pm$ 0.7	-0.2 $\pm$ 1.0	0.4
	U		0.1 $\pm$ 0.3	0.7 $\pm$ 0.1	0.3 $\pm$ 0.9	1.0
	XCO <sub>2</sub>		0.1 $\pm$ 0.2	0.6 $\pm$ 0.4	0.1 $\pm$ 0.9	0.7

1421

1422 Table 3. Standard deviations versus aircraft showing the errors resulting

1423 from imperfect co-location, GOSAT predicted error, and GOSAT error (for

1424 single observations). The next sets are the true variability, 15-observation

1425 averages of prior error and GOSAT error. The GOSAT and prior standard

1426 deviation have the co-location error subtracted.

Type		Ocean surface (ppm)	HIPPO Ocean (ppm)	ESRL Ocean (ppm)	ESRL Land (ppm)	AJAX Land (ppm)
colocation standard deviation	LMT	0.5 $\pm$ 0.2	0.3 $\pm$ 0.1	0.3 $\pm$ 0.1	2.1 $\pm$ 0.7	1.1
	U	0.9 $\pm$ 0.4	0.1 $\pm$ 0.1	0.2 $\pm$ 0.0	0.5 $\pm$ 0.3	0.1
	XCO <sub>2</sub>		0.1 $\pm$ 0.2	0.2 $\pm$ 0.1	0.8 $\pm$ 0.3	0.2



<b>predicted error (n=1)</b>	LMT	4.3±0.2	4.3±0.3	4.3±0.1	4.6±0.3	4.1
	U		1.7±0.1	1.7±0.0	1.8±0.0	1.7
	XCO <sub>2</sub>		0.6±0.1	0.7±0.1	0.9±0.1	0.8
<b>GOSAT standard deviation (n=1)</b>	LMT	1.7±0.4	1.7±0.3	1.5±0.1	3.4±0.7	2.9
	U		0.8±0.1	0.8±0.0	1.3±0.3	1.1
	XCO <sub>2</sub>		0.9±0.1	0.8±0.1	1.7±0.4	0.9
<b>true variability</b>	LMT	1.3±0.8	0.6± 0.2	0.9±0.6	5.5±2.0	2.8
	U		0.4±0.3	0.8±0.8	2.0±0.2	2.0
	XCO <sub>2</sub>		0.3±0.3	0.8±0.8	2.5±0.6	2.4
<b>prior standard deviation (n=15)</b>	LMT	2.2±0.9	0.5± 0.3	0.7±0.2	2.1±1.0	-
	U		0.3±0.1	0.5±0.0	0.9±0.2	-
	XCO <sub>2</sub>		0.3±0.1	0.5±0.1	1.1±0.6	-
<b>GOSAT standard deviation (n=15)</b>	LMT	0.4±0.3	0.5± 0.1	0.4±0.1	1.9±1.1	-
	U		0.4±0.1	0.6±0.1	0.7±0.4	-
	XCO <sub>2</sub>		0.3±0.1	0.4±0.1	0.8±0.5	-

1427

1428

1429

Table 4. Estimated co-location, correlated, and random errors. The co-location errors are the same as in Table 3.

	Type	Ocean surface (ppm)	HIPPO Ocean (ppm)	ESRL Ocean (ppm)	ESRL Land (ppm)
<b>colocation standard deviation</b>	LMT	1.0±0.4	0.3±0.1	0.3±0.1	2.1±0.7
	U		0.1±0.1	0.2±0.0	0.5±0.3
	XCO <sub>2</sub>		0.1±0.1	0.1±0.1	0.8±0.3
<b>correlated error (a<sub>o</sub>)</b>	LMT	0.4±0.3	0.3±0.2	0.3±0.2	1.7±1.3
	U		0.3±0.2	0.5±0.1	0.6±0.4
	XCO <sub>2</sub>		0.2±0.2	0.4±0.1	1.1±0.6
<b>random error (b)</b>	LMT	1.6±0.4	1.6±0.3	1.4±0.2	3.0±0.6
	U		0.8±0.1	0.6±0.1	1.2±0.1
	XCO <sub>2</sub>		0.9±0.1	0.4±0.1	0.8±0.3

1430

1431

1432

1433

1434

1435

Table 5. Enhancements in CO and CO<sub>2</sub> for May and August, 2010. The target box is 11 to 18S, 60 to 56W for May, and 55-60S, 13-17W for August. The CO background box is 11 to 18S, 40 to 44W for May and 157.8-161.8W, 19-23S for August. Rarotonga aircraft measurements are used for CO<sub>2</sub> background.

		CO				GOSAT LMT CO <sub>2</sub>		
		backg rnd (ppb)	Target all (ppb)	Target DOFs > 0.15) (ppb)	Target (DOFs > 0.25) (ppb)	Target (DOFs > 0.30) (ppb)	backgrnd from RTA (ppm)	Target (DOFs = 0.8)
<b>May, 2010</b>	Mean	68±9	122±49	123±54	146±77	182±96	386.4	389.6±2.3
	N	1502	2023	1556	500	215		13
	DOFs		0.21	0.24	0.32	0.39		0.85
	ΔCO or ΔCO <sub>2</sub>	-	54	55	88	114	-	3.2



<b>August, 2010</b>	Mean	91±22	305±171	311±180	336±200	372±221	387.4	392.2±6.7
	N	2989	3881	3227	1887	1231	-	5
	$\Delta\text{CO}$ or $\Delta\text{CO}_2$	-	213.7	219.3	244.8	281.1	-	4.8

1436

1437 Table 6a. Bias terms for LMT – U. Compare to Table 2.

	<b>HIPPO Ocean (ppm)</b>	<b>ESRL Ocean (ppm)</b>	<b>ESRL Land (ppm)</b>
<b>colocation bias</b>	-0.4±0.2	-0.2±0.3	-0.6±0.5
<b>true mean</b>	1.1±0.8	0.4±0.5	1.0±2.7
<b>prior bias</b>	-1.0±1.3	-2.8±2.9	-1.0±1.2
<b>GOSAT bias</b>	0.0±0.4	-0.5±0.9	-0.5±0.8

1438

1439 Table 6b. Standard deviations for LMT – U. Compare to Table 3. The  
1440 predicted errors in the table use the errors given at the end of Section 5.1.5.

	<b>HIPPO Ocean (ppm)</b>	<b>ESRL Ocean (ppm)</b>	<b>ESRL Land (ppm)</b>
<b>colocation stdev</b>	0.3±0.1	0.3±0.1	2.1±0.7
<b>predicted error (n=1)</b>	1.2±0.0	1.2±0.0	2.7±0.0
<b>GOSAT stdev (n=1)</b>	1.5±0.4	1.3±0.1	2.3±0.5
<b>true variability</b>	0.5± 0.2	0.8±0.1	4.8±1.5
<b>prior stdev (n=15)</b>	0.5± 0.2	0.8±0.1	1.4±0.8
<b>GOSAT stdev (n=15)</b>	0.5± 0.2	0.7±0.1	1.2±0.8

1441

1442 Table 6c. Error fits for LMT – U. Compare to Table 4.

	<b>HIPPO Ocean (ppm)</b>	<b>ESRL Ocean (ppm)</b>	<b>ESRL Land (ppm)</b>
<b>colocation stdev</b>	0.3±0.1	0.3±0.1	2.1±0.7
<b>correlated (a)</b>	0.4±0.2	0.6±0.0	0.9±0.9
<b>random (b)</b>	1.4±0.4	1.1±0.1	2.1±0.7

1443

1444 Table A.1 Filtering and Bias corrections

<b>parameter</b>	<b>ocean filtering</b>	<b>ocean bias correction</b>	<b>land filtering</b>	<b>land bias correction</b>
albedo_2	0.0215 < val < 0.024	-1272.02 ± 50	-	-
albedo_slope_2	val < 8e-6	-	-	-
aod_dust	val < 0.01	-	-	-36.03 ± 1
aod_total	val < 0.25	-	-	-
h2o_ratio	0.96 < val < 1.02	-	-	-
co2_grad_delta	-40 < val < 17	0.396330 ± 0.004	-	0.310 ± 0.003
constant	-	52.674 ± 6	-	0.01259 ± 0.4
b1_offset	-	-1.25204 ± 0.05	-	-
surfacepressure_xa	-	-0.0381105 ± 0.006	-	-
s32	-	17.0742 ± 3	-	-
surfacepressurediff	-	0.869280 ± 0.05	-	-
albedo_1	-	144.458 ± 9	-	-
co2_grad_delta_prime	-	-0.171350 ± 0.01	-	-0.027 ± 0.005
dofs_LMT	-	-	val > 0.68	-



xco2_error	-	-	val < 1.4	6.02 ± 0.3
albedo_slope_3	-	-	-1.5e-4 < val < 2.0e-4	-
xco2_dofs	-	-	val > 1.3	-
ice_height	-	-	val > -0.1	-
surfacePressureDiff	-	-	-4 < val < 2	-
albedo_3	-	-	-	-11.66 ± 0.7
dp_cld	-	-	-	0.219 ± 0.01

1445 \* parameters also used in ACOS-GOSAT XCO<sub>2</sub> bias correction

1446

1447 Table A2a. Effects of bias corrections and quality flags on land comparisons  
 1448 (ESRL aircraft land observations)

	n	lmt bias (ppm)	lmt bias var. (ppm)	lmt stdev (ppm)	u bias var. (ppm)	u stdev (ppm)
original (XCO <sub>2</sub> flags)	15143	13.54	2.79	7.70	1.61	3.05
all quality flags (see appendix A)	12714	13.37	2.30	7.55	1.27	2.98
bias correction (see appendix A)	12714	-1.18	1.43	3.47	0.79	1.36
fit U separately	11978	-	-	-	0.70	1.43

1449

1450 Table A2b. Effects of bias corrections and quality flags on ocean  
 1451 comparisons (HIPPO and ESLR ocean dataset stations/campaigns: tgc, rta,  
 1452 aoa, 2S, 2N, 3S, 3N, 4S, 4N, 5S, 5N)

	n	lmt bias (ppm)	lmt bias var. (ppm)	lmt stdev (ppm)	u bias var. (ppm)	u stdev (ppm)
original (XCO <sub>2</sub> flags)	9836	1.73	3.46	3.77	0.78	0.85
with cutoffs (see Appendix A)	6143	1.47	1.92	3.18	0.63	0.69
bias correction (see Appendix A)	6143	0.04	0.68	1.60	0.38	0.79
fit U separately	6143	-	-	-	0.35	0.60

1453

1454 The fit parameters are tested for robustness by using a subset of the dataset  
 1455 to determine the fit and then testing the fit on the independent subset. For  
 1456 the ocean data, HIPPO campaigns 2N, 3S, 4, and 5 are used to develop bias  
 1457 correction, and HIPPO 2S and 3N are used for testing. For land data,  
 1458 stations bne, car, cma, dnd, esp, etl, hil, hip, are used for development, and  
 1459 stations lef, nha, pfa, sca, sgp, tgc, thd, wbi are used for testing.

1460

1461 Table A3a: Ocean bias correction robustness test. Comparisons to aircraft  
 1462 data are tested using (a) no bias correction, (b) bias correction using the  
 1463 test dataset, (c) an independent dataset, and (d) the entire dataset

Bias correction testing	Mean bias	Bias std	mean std
no correction	0.69	0.69	2.97
subset tested on itself	-0.04	0.33	1.47
independent subset	-0.26	0.46	1.58
all data used	-0.14	0.49	1.54





1464

1465 Table A3b: Land bias correction robustness test. Same as Table A3a but for  
 1466 land.

Bias correction testing	Mean bias	Bias std	mean std
no correction	13.00	2.47	7.54
subset tested on itself	0.16	1.55	3.68
independent subset	1.05	1.24	3.67
all data used	0.50	1.51	3.65

1467

1468 Table A4: Effect of profile extension. GOSAT corrected as described in  
 1469 Table A1 and compared to aircraft data with profile extended 4 different  
 1470 ways: (a) using the GOSAT prior, (b) extending the aircraft to the  
 1471 tropopause pressure, with the GOSAT prior above this, (c) using the CT2015  
 1472 model, and (d) extending the aircraft to the tropopause pressure, with the  
 1473 CT2015 above this

Profile extension	LMT bias	LMT Bias std	LMT std	U bias	U Bias std	U std
(a) prior	-0.90	1.37	3.46	-0.38	0.70	1.25
(b) extend+prior	-0.99	1.44	3.47	-0.20	0.79	1.35
(c) CT2015	-1.20	1.39	3.47	-0.02	0.66	1.26
(d) extend+CT2015	-1.18	1.43	3.47	-0.05	0.79	1.36

1474

1475 Table B1. Actual and predictions of errors by station/campaign. Columns *a*  
 1476 and *b* are the fits to actual errors when averaging using Eq. 11a;  $\varepsilon_{coloc}$  is the  
 1477 standard deviation of CT2015 at the observation vs. validation data. The  
 1478 predicted error is the error calculated from the ACOS full error covariance for  
 1479 each type of quantity. Bias ct\_ct is difference between CT2015 at the  
 1480 satellite and validation locations. True mean is the average validation value  
 1481 at each location; prior and GOSAT biases are difference between the prior  
 1482 and retrieved GOSAT minus validation data. The last three columns are the  
 1483 standard deviation of the true, prior minus true, and GOSAT retrieved minus  
 1484 true for 15 observation averages.  
 1485

location	latitude, longitude	$\varepsilon_{coloc}$ ct_ct stdev	a corr. error	b rand. error	GOSAT prior (n=1)	GOSAT stdev (n=1)	pred. Error (n=1)	bias ct_ct	true mean	prior bias	GOSAT bias	true stdev (n=1)	prior stdev (n=15)	GOSAT stdev (n=15)
a) LMT vs. surface ocean flasks at remote sites														
		(ppm)	(ppm)	(ppm)	(ppm)	(ppm)	(ppm)	(ppm)	(ppm)	(ppm)	(ppm)	(ppm)	(ppm)	(ppm)
bmw	32N,65W	0.4	0.9	2.5	4.6	2.6	4.2	-0.8	391.8	-3.0	-1.4	3.3	2.8	1.1
mid	28N,177W	0.8	1.5	1.8	4.2	2.3	4.3	0.1	389.9	-2.4	-0.2	2.2	4.5	1.5
mnm	24N,154E	0.3	0.8	1.6	3.8	1.8	4.2	0.2	393.2	-3.8	-0.6	1.6	2.8	0.9
mlo	20N,156W	0.8	1.0	1.4	2.6	1.7	4.5	-0.6	390.9	-2.1	-0.3	1.7	2.2	1.0
kum	20N,155W	0.7	1.5	1.2	2.6	1.9	4.5	-0.6	390.0	-1.1	0.7	1.7	2.5	1.5
gmi	13N,145E	0.5	0.7	1.6	2.8	1.8	4.4	0.0	394.8	-2.9	0.9	1.2	1.9	0.8
chr	2N,157W	0.3	0.8	1.4	1.6	1.6	4.4	-0.2	392.1	-0.8	0.4	1.1	1.9	0.9
sey	5S,56E	0.4	1.3	1.8	2.2	2.2	4.0	-0.3	391.4	-0.2	0.7	1.3	0.8	1.3
asc	8S,14W	0.3	1.0	1.5	1.7	1.8	4.4	-0.4	390.4	0.1	1.5	0.7	2.5	1.1
sno	14S,171W	0.5	0.5	1.7	2.2	1.8	4.2	-0.5	390.6	0.0	0.6	0.5	2.2	0.7





sca	33N,79W	0.3	0.3	1.5	0.7	1.6	0.9	-0.2	392.7	0.2	-0.9	1.7	0.6	0.5
aoa	29N,148E	0.2	0.5	0.6	0.5	0.8	0.6	-0.2	392.4	-1.2	0.3	1.4	0.5	0.6
tgc	28N,97W	0.4	0.5	1.2	0.9	1.4	0.7	0.0	392.3	0.3	-0.3	1.9	0.9	0.6
rta	21S,160W	0.1	0.3	0.8	0.5	0.9	0.7	0.0	390.3	2.0	0.8	0.2	0.4	0.4
<b>average</b>		<b>0.8</b>	<b>1.0</b>	<b>1.6</b>	<b>1.5</b>	<b>1.9</b>	<b>0.9</b>	<b>-0.1</b>	<b>391.5</b>	<b>-0.3</b>	<b>-0.0</b>	<b>2.5</b>	<b>1.3</b>	<b>1.1</b>
<b>land</b>		<b>±0.3</b>	<b>±0.5</b>	<b>±0.2</b>	<b>±0.4</b>	<b>±0.4</b>	<b>±0.1</b>	<b>±0.3</b>	<b>±1.1</b>	<b>±0.6</b>	<b>±0.9</b>	<b>±0.6</b>	<b>±0.6</b>	<b>±0.5</b>
<b>ave. land, corrected</b>			<b>0.7</b>		<b>0.5</b>	<b>1.7</b>				<b>-0.2</b>	<b>0.1</b>		<b>1.1±0.6</b>	<b>0.6</b>
			<b>±0.5</b>		<b>±0.0</b>	<b>±0.4</b>				<b>±0.6</b>	<b>±0.9</b>			<b>±0.5</b>
<b>aoa, rta</b>	<b>average</b>	<b>0.2</b>	<b>0.4</b>	<b>0.7</b>	<b>1.1</b>	<b>0.9</b>	<b>0.7</b>	<b>-0.1</b>	<b>391.4</b>	<b>0.4</b>	<b>0.6</b>	<b>0.8</b>	<b>0.5</b>	<b>0.5</b>
	<b>ocean</b>	<b>±0.1</b>	<b>±0.1</b>	<b>±0.1</b>	<b>±0.4</b>	<b>±0.1</b>	<b>±0.1</b>	<b>±0.1</b>	<b>±1.5</b>	<b>±2.3</b>	<b>±0.4</b>	<b>±0.8</b>	<b>±0.1</b>	<b>±0.1</b>
<b>e) LMT GOSAT HIPPO ocean</b>														
2S	30S-0S	0.3	0.3	1.5	0.5	1.5	4.0	-0.1	390.9	2.0	-0.4	0.5	0.4	0.5
2N	15S-5S	0.4	0.3	1.6	0.5	1.6	4.1	-0.1	390.7	2.2	-0.2	0.4	0.5	0.5
3S	10S-10N	0.2	0.0	2.4	0.7	2.4	4.3	-0.4	393.5	-0.1	0.0	1.2	0.3	0.6
3N	5S-10N	0.5	0.3	1.9	0.5	1.9	3.9	-0.4	393.4	-0.1	-0.4	0.6	0.4	0.6
4S	10N	0.1	0.5	1.5	0.5	1.6	4.6	-0.5	394.5	-3.0	0.2	0.3	0.4	0.6
4N	15-30N	0.3	0.4	1.5	1.2	1.5	4.2	-0.3	393.4	-4.2	-0.5	0.5	0.8	0.5
5S	0-20N	0.4	0.6	1.5	1.4	1.6	4.5	-0.2	390.7	-0.1	-0.4	0.6	1.0	0.7
5N	10S-20N	0.5	0.5	1.3	1.1	1.4	4.5	-0.3	390.6	2.0	0.3	0.7	0.8	0.6
	<b>average</b>	<b>0.3</b>	<b>0.4</b>	<b>1.6</b>	<b>0.8</b>	<b>1.7</b>	<b>4.3</b>	<b>-0.3</b>	<b>392.2</b>	<b>-0.2</b>	<b>-0.2</b>	<b>0.6</b>	<b>0.6</b>	<b>0.6</b>
		<b>±0.1</b>	<b>±0.2</b>	<b>±0.3</b>	<b>±0.4</b>	<b>±0.3</b>	<b>±0.3</b>	<b>±0.2</b>	<b>±1.6</b>	<b>±2.4</b>	<b>±0.3</b>	<b>±0.3</b>	<b>±0.3</b>	<b>±0.6</b>
<b>f) U GOSAT HIPPO ocean</b>														
2S	30S-0S	0.1	0.6	0.8	0.4	1.0	1.6	0.1	390	2.6	0.1	0.3	0.4	0.7
2N	15S-5S	0.2	0.2	0.7	0.2	0.7	1.6	0.1	390.1	2.6	0.7	0.2	0.2	0.2
3S	10S-10N	0.1	0.3	0.9	0.6	1.0	1.7	0.0	391.6	0.9	0.3	1.0	0.6	0.4
3N	5S-10N	0.3	0.1	0.8	0.4	0.8	1.6	0.1	391.1	1.3	0.4	0.4	0.3	0.2
4S	10N	0.1	0.2	0.8	0.2	0.8	1.8	0.3	392.8	-0.2	0.2	0.2	0.2	0.3
4N	15-30N	0.1	0.2	0.7	0.3	0.7	1.6	-0.1	392.9	-0.3	0.2	0.2	0.2	0.3
5S	0-20N	0.1	0.3	0.8	0.3	0.9	1.8	0.1	390.4	1.2	-0.2	0.2	0.2	0.4
5N	10S-20N	0.2	0.3	0.7	0.3	0.8	1.8	0.1	390.2	1.8	0.0	0.3	0.2	0.4
	<b>average</b>	<b>0.1</b>	<b>0.3</b>	<b>0.8</b>	<b>0.3</b>	<b>0.8</b>	<b>1.7</b>	<b>0.1</b>	<b>391.1</b>	<b>0.3</b>	<b>0.2</b>	<b>0.4</b>	<b>0.3</b>	<b>0.4</b>
		<b>±0.1</b>	<b>±0.2</b>	<b>±0.1</b>	<b>±0.1</b>	<b>±0.1</b>	<b>±0.1</b>	<b>±0.1</b>	<b>±1.2</b>	<b>±1.1</b>	<b>±0.3</b>	<b>±0.3</b>	<b>±0.1</b>	<b>±0.1</b>
<b>g) XCO<sub>2</sub> GOSAT HIPPO ocean</b>														
2S	30S-0S	0.1	0.4	0.8	0.2	0.9	0.5	0.0	390.2	2.5	0.0	0.2	0.2	0.5
2N	15S-5S	0.1	0.0	0.7	0.2	0.7	0.5	0.0	390.2	2.5	0.5	0.2	0.2	0.2
3S	10S-10N	0.1	0.2	1.1	0.6	1.1	0.7	-0.1	392.0	0.6	0.2	1.1	0.5	0.3
3N	5S-10N	0.3	0.0	0.9	0.4	0.9	0.5	0.0	391.6	1.0	0.2	0.5	0.2	0.2
4S	10N	0.1	0.3	0.9	0.2	0.9	0.8	0.1	393.2	-0.9	0.2	0.2	0.2	0.4
4N	15-30N	0.1	0.1	0.7	0.3	0.8	0.6	-0.1	393.1	-1.2	0.0	0.2	0.1	0.2
5S	0-20N	0.1	0.3	0.9	0.5	1.0	0.7	0.0	390.5	0.9	-0.2	0.3	0.3	0.4
5N	10S-20N	0.2	0.3	0.8	0.5	0.8	0.8	0.0	390.3	1.8	0.0	0.3	0.3	0.4
	<b>average</b>	<b>0.1</b>	<b>0.2</b>	<b>0.9</b>	<b>0.4</b>	<b>0.9</b>	<b>0.6</b>	<b>0.0</b>	<b>391.4</b>	<b>0.9</b>	<b>0.1</b>	<b>0.4</b>	<b>0.3</b>	<b>0.3</b>
		<b>±0.2</b>	<b>±0.2</b>	<b>±0.1</b>	<b>±0.2</b>	<b>±0.1</b>	<b>±0.1</b>	<b>±0.1</b>	<b>±1.3</b>	<b>±1.4</b>	<b>±0.2</b>	<b>±0.3</b>	<b>±0.1</b>	<b>±0.1</b>
<b>h) AJAX</b>														
LMT		1.1			2.2	3.1	4.1	-0.6	393.6	-2.0	-0.2	2.8		
LMT, corrected*					1.9	2.9				-1.4	+0.4			
U		0.1			0.9	1.1	1.7	0.0	392.2	0.4	1.0	2.0		
XCO <sub>2</sub>		0.2			0.6	0.9	0.8	-0.1	392.4	-0.1	0.7	2.4	-	-

1486 \*AJAX profiles are co-located within 1 hour and 1 degree and therefore do not have multiple GOSAT  
 1487 matches to average.

1488

1489

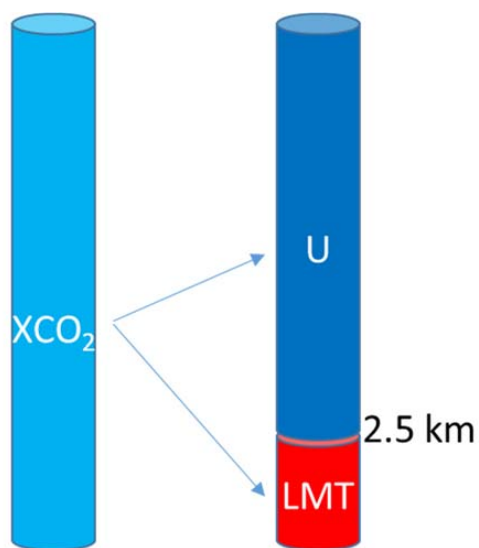


Figure 1. XCO<sub>2</sub> full column measurement (left) and the two partial columns that we introduce (right): the lowermost troposphere (LMT), a partial column from the surface to approximately 2.5 km, and the partial column above 2.5 km (U).

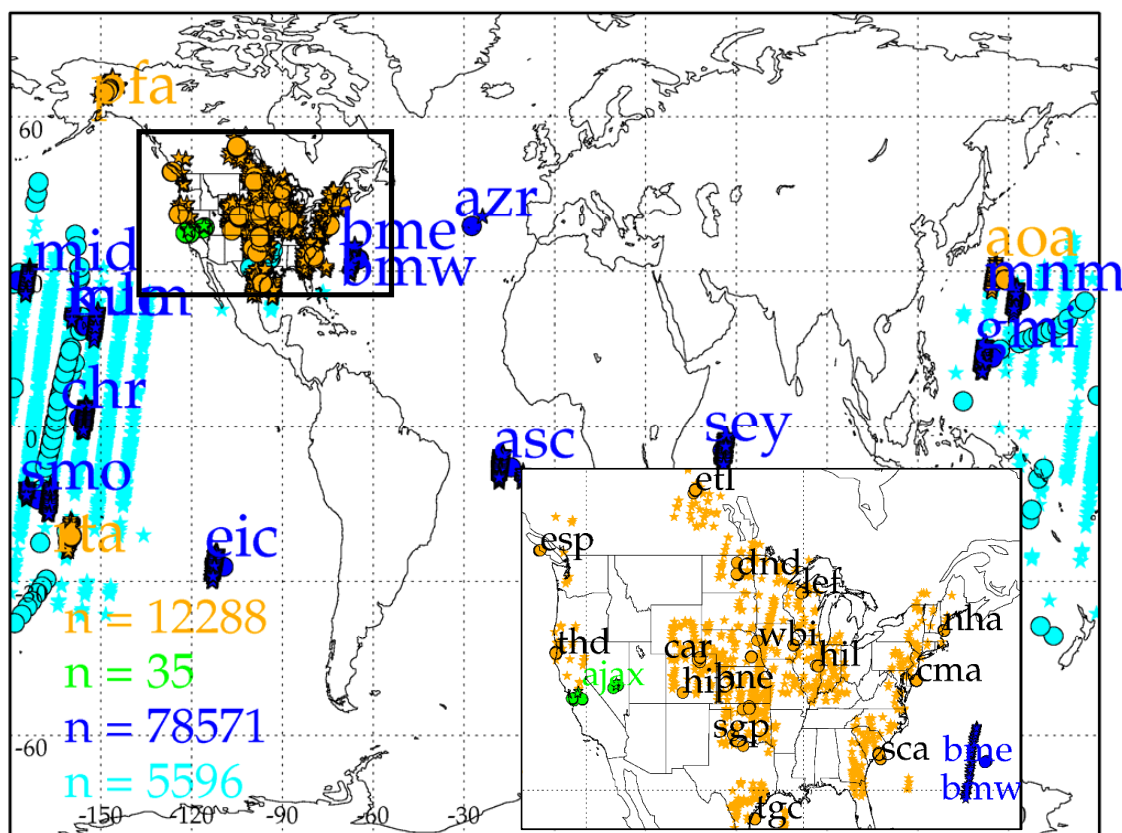


Figure 2. Validation locations. The 4 sets of validation data shown here are: ESRL aircraft (orange), which has both land (in the US) and ocean (RTA and AOA), AJAX aircraft data (green) in the western U.S., the HIPPO aircraft campaign (light blue), and remote ocean surface sites (dark blue). The matching GOSAT locations are shown as stars and the validation locations are shown as outlined circles. The number of GOSAT observations in each set are shown as the "n =" number in the lower left of the plot.

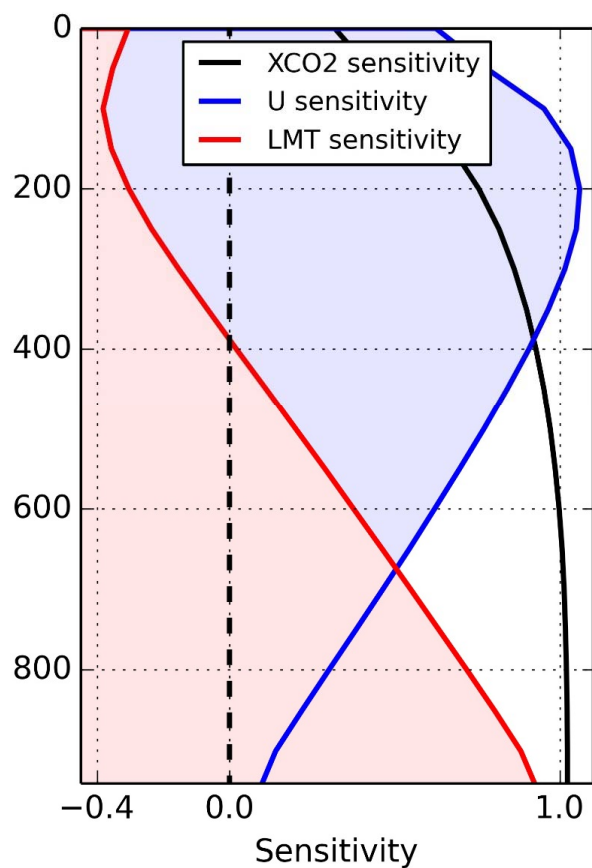


Figure 3. Sensitivity of XCO<sub>2</sub> (black), partitioned into the LMT (red) and U (blue) partial columns for an average land averaging kernel. The LMT sensitivity is approximately 1 near the surface and drops off steadily with decreasing pressure. The ocean averaging kernel is very similar.

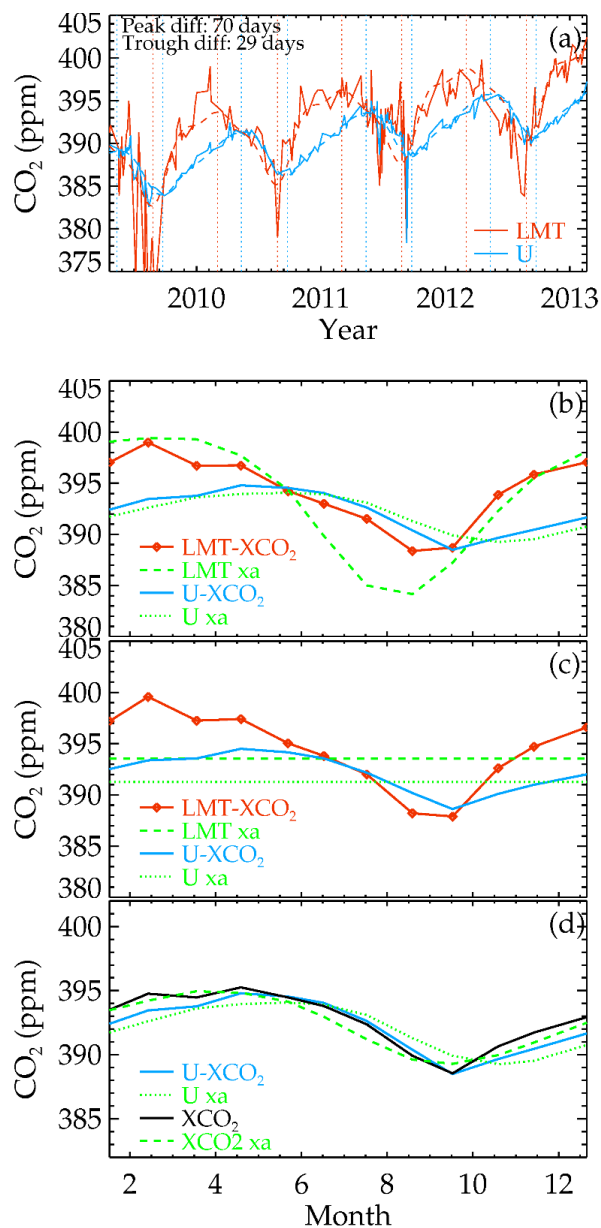


Figure 4. Simulated GOSAT retrievals from SGP aircraft profiles, Eqs. 5-6, and the GOSAT averaging kernels. (a) Time series of LMT (red) and U (blue) with dashed lines the monthly averages; (b) seasonal cycle (created by moving all measurements to be in 2012 by offsetting CO<sub>2</sub> by 2 ppm per year), averaging in 1-month increments. Dotted and dashed lines are initial guess/a priori. (c) same as (b) except that the prior is set to a constant (with 2 ppm/year secular increase), showing that LMT and U results are not strongly influenced by the prior. (d) Same as (b) but showing U (blue) vs. XCO<sub>2</sub> (black) which shows that XCO<sub>2</sub> estimates look most similar to the U partial column. Analysis in Section 3.3 shows that 70% of XCO<sub>2</sub> variations result from variations in the U partial column.

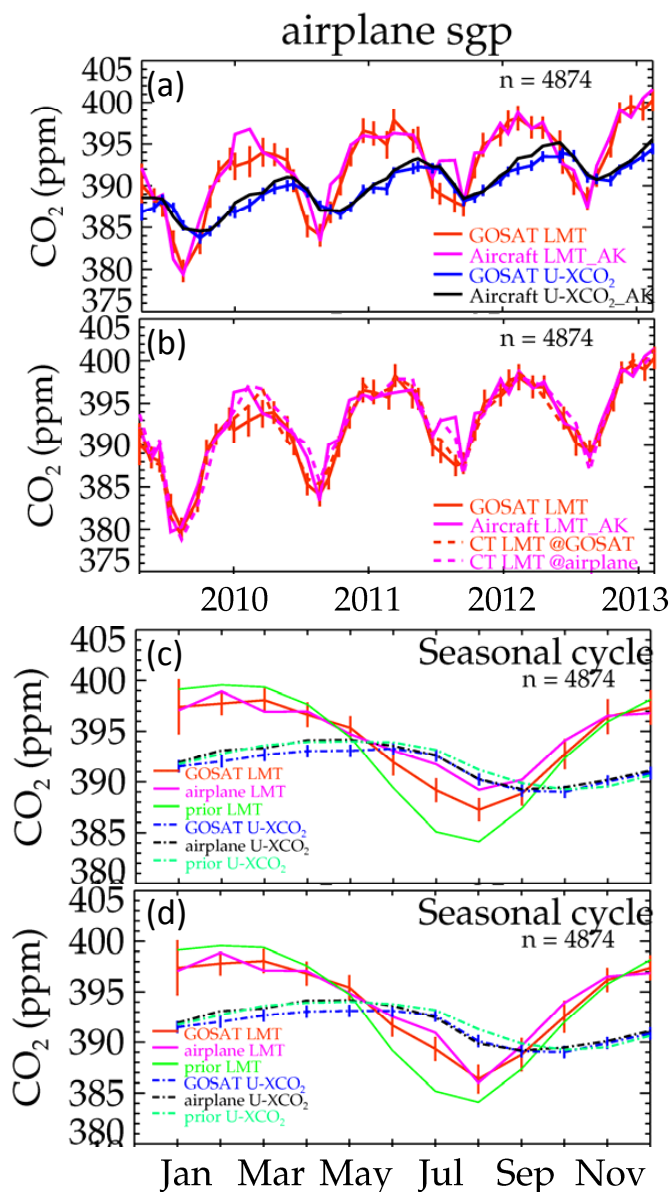


Figure 5. GOSAT versus aircraft data at the SGP site (37N, 95W). (a) aircraft LMT (pink) and U (blue) versus GOSAT LMT (red) and U (black) for monthly averages of GOSAT/airplane matches. (b) same as (a) but also showing CarbonTracker matched to GOSAT (red dotted) and CarbonTracker matched to aircraft (pink dotted) for LMT. (c) Seasonal cycle of GOSAT and airplane, same colors as top panel, and adding the priors in green. (d) Same as (c) but removing months where the CarbonTracker difference from (b) is larger than 2.5 ppm (removing months 6/9, 10/9, 5/10, 7/10, 8/10). This shows that the systematic monthly differences in panel (c) result from co-location error. In (c) and (d), the GOSAT prior overestimates the high and overestimates the drawdown. For all metrics except for the U bias, GOSAT LMT and U improve over the prior estimates.



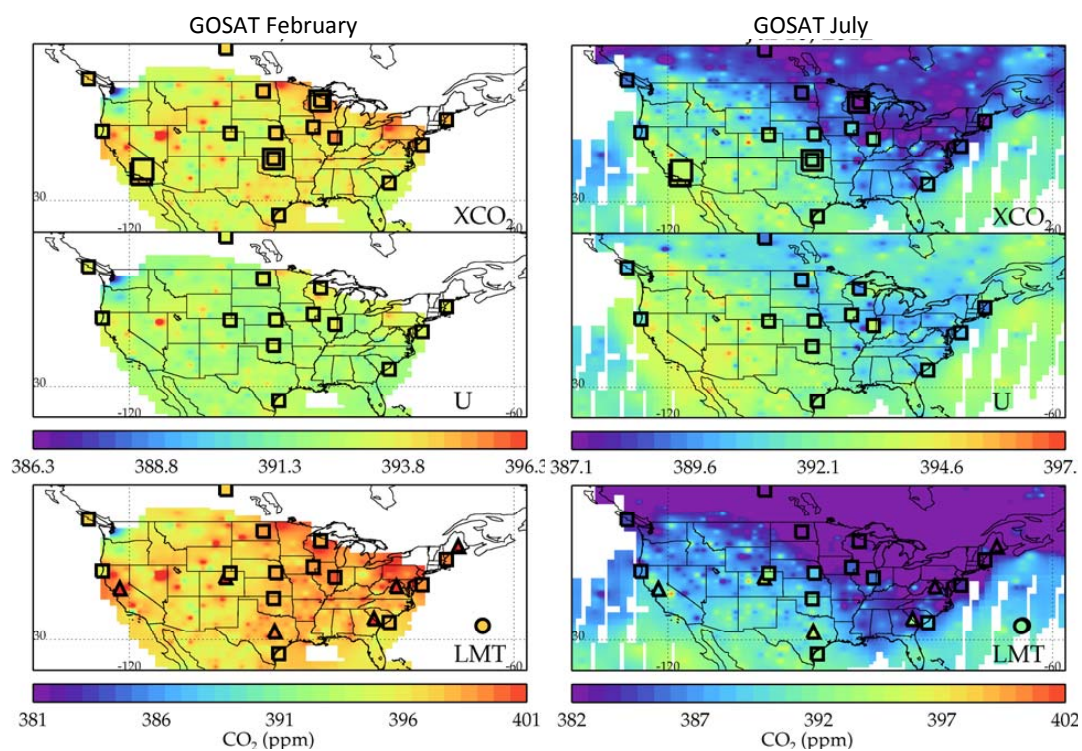


Figure 6. GOSAT XCO<sub>2</sub> (top), U (middle), and LMT (bottom) in February (left) and July (right). Aircraft with GOSAT averaging kernels are small squares, towers are triangles, remote ocean surface sites are circles, and TCCON are large squares (only shown on XCO<sub>2</sub> panels). Data is averaged over the GOSAT record (converted to 2012 by adding/subtracting 2 ppm per year).

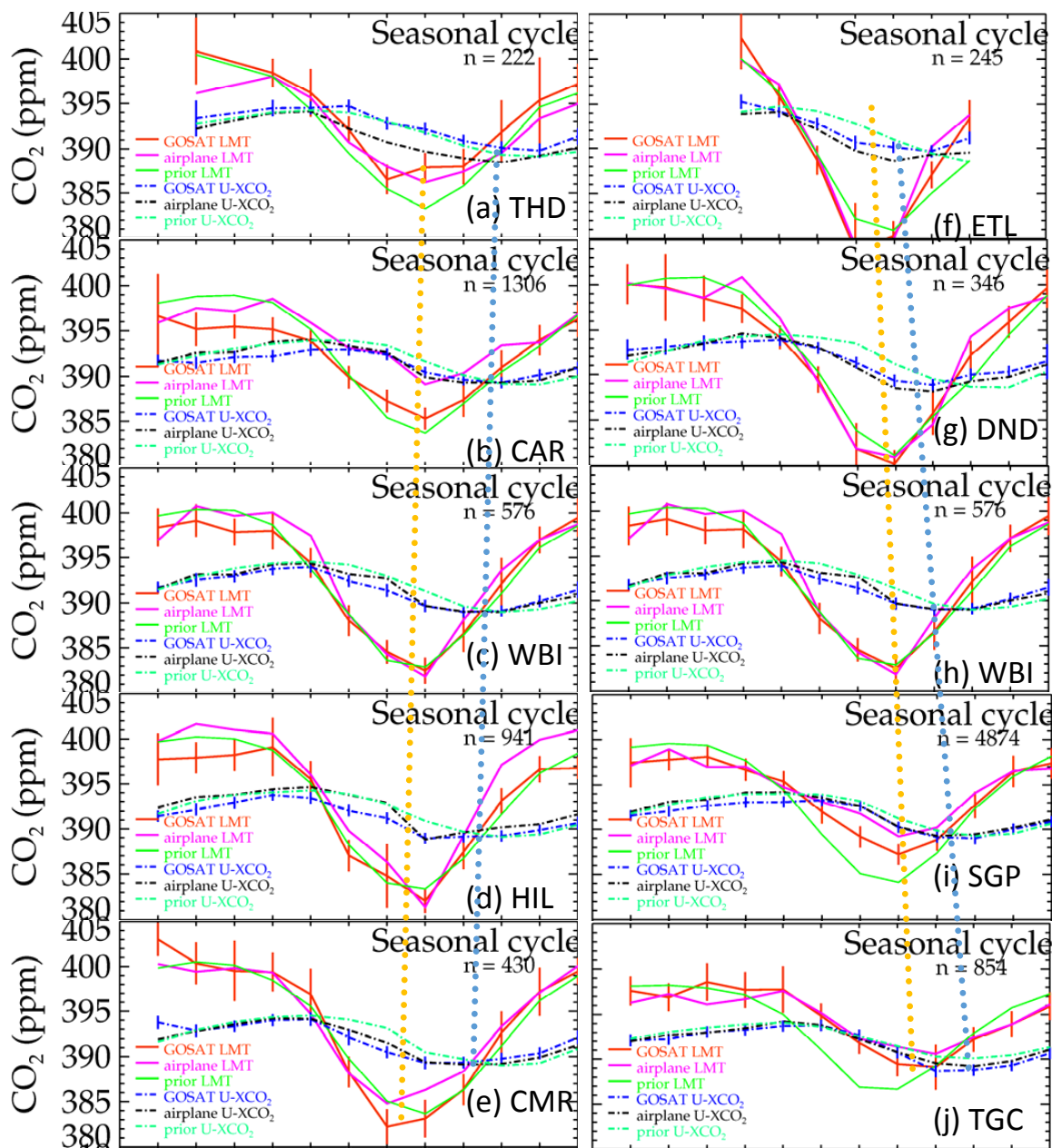


Figure 7. Seasonal cycle at 5 sites arranged from north to south (a-e) and west to east (f-j). The seasonal cycle minimum is marked for LMT (orange) and U (blue). The seasonal cycle shifts forward going west and backwards going north, for both LMT and U. There is a consistent delay in the drawdown for the U prior for (b-j) which is corrected by the retrieval. The LMT prior is consistently too large for (i-j) with a phase shift in (j) which is corrected by the GOSAT retrieval.

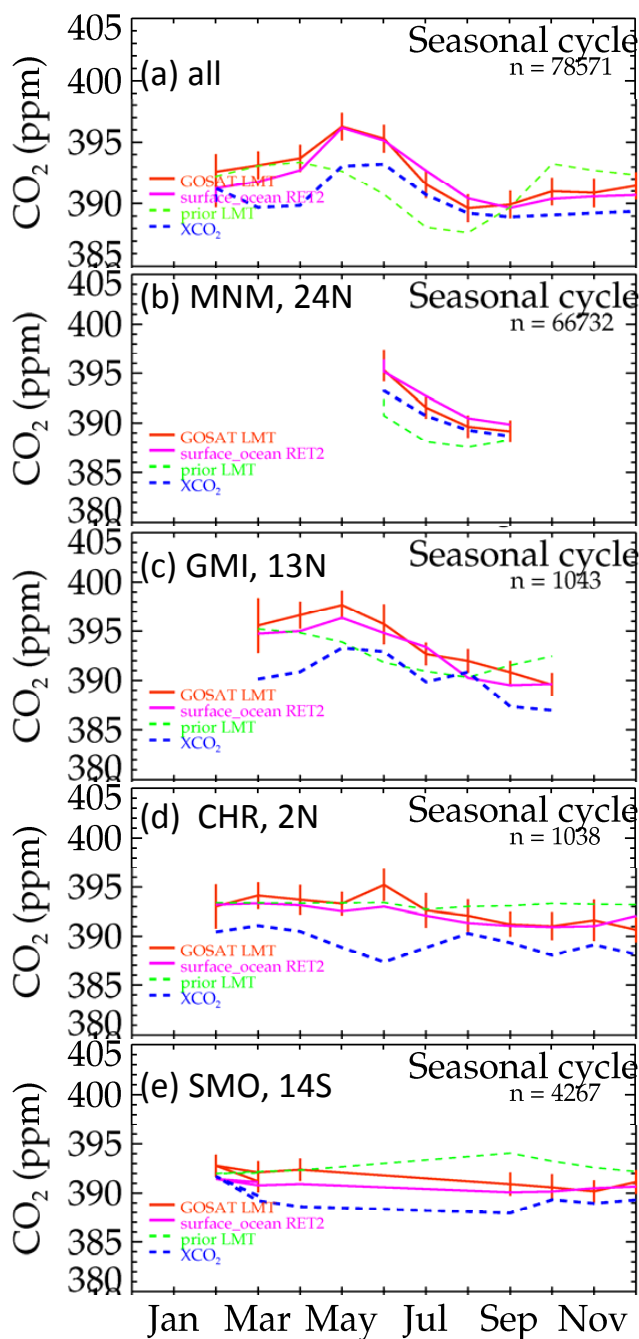


Figure 8. GOSAT LMT compared with remote ocean surface sites for different sites. GOSAT (red) compares well with surface site (pink) for the average of all sites (a) and at the four (of twelve) sites with the most matches (b-e). There is marked improvement over the prior (green). XCO<sub>2</sub> values are shown for comparison (blue dashed).

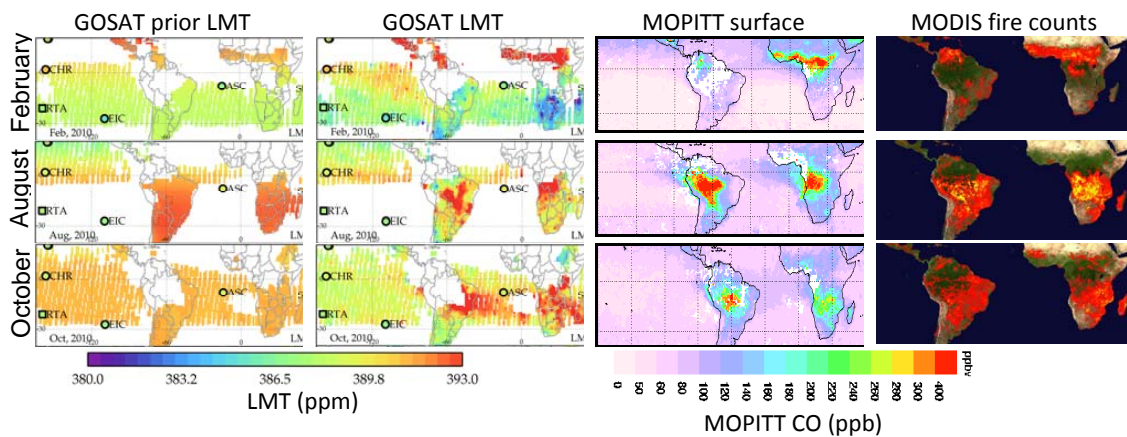


Figure 9. GOSAT LMT versus MOPITT and MODIS fire counts in for February, August, and October, 2010. GOSAT prior (left) and retrieved (second column) LMT compared with MOPITT multispectral CO (third column) and MODIS fire counts (right). The GOSAT prior is approximately constant in the southern hemisphere on monthly timescales. GOSAT LMT shows the pattern of biomass burning in South America and Africa seen by MOPITT and MODIS and reduces from the prior in the Pacific, matching surface and aircraft observations. Note that multi-spectral MOPITT retrievals have little surface sensitivity over ocean, but the outflow seen in October is seen in mid-tropospheric MOPITT.

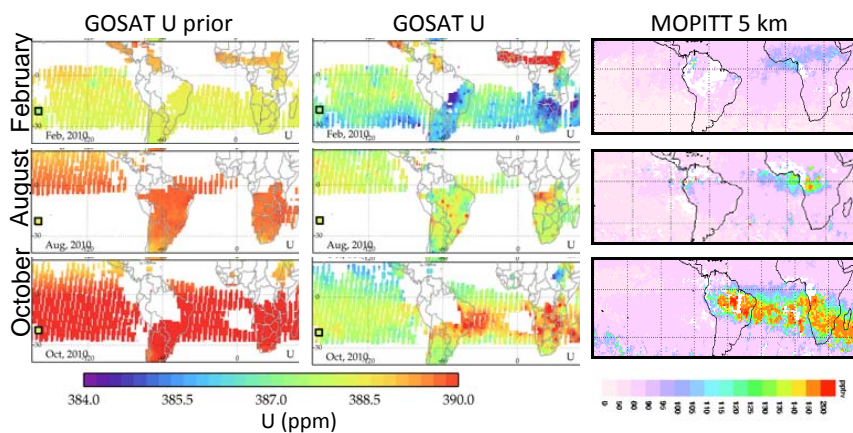


Figure 10. GOSAT U versus MOPITT for February, August, and October, 2010. GOSAT prior (left) and retrieved (middle) compared with MOPITT multispectral CO (right) at 5 km. The GOSAT prior is approximately constant in the southern hemisphere on monthly timescales. GOSAT U shows low CO<sub>2</sub> from the growing season for the Amazon and southern Africa in February. In August, GOSAT U shows little enhancement in South America, but enhancement in southern Africa, in agreement with MOPITT. In October, GOSAT U shows enhancement over the burning regions and outflow similar to MOPITT.

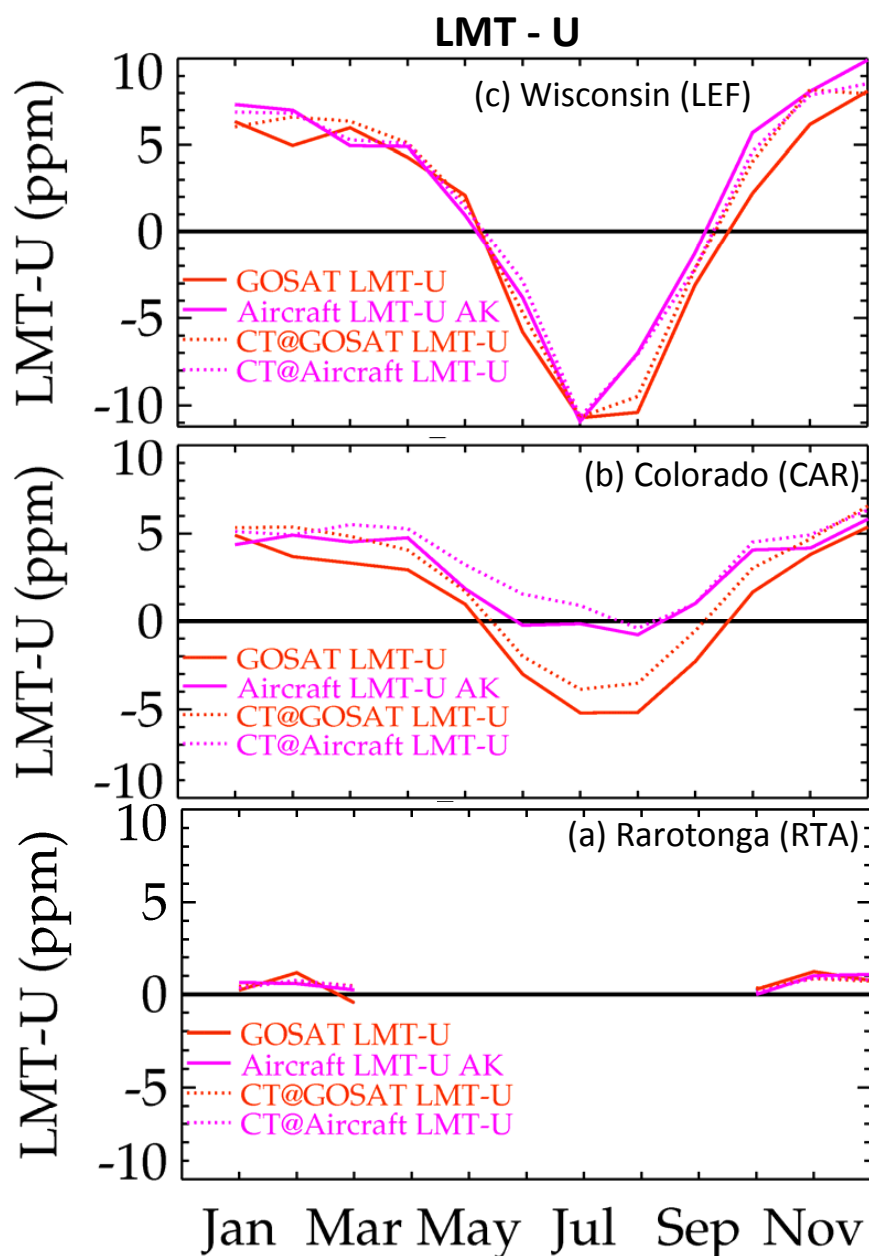


Figure 11. GOSAT LMT - U (red) versus aircraft (pink) at 3 sites. The dotted line show CarbonTracker matched to GOSAT (red dotted) or aircraft (pink dotted). Co-location error explains the discrepancies in the drawdown at CAR and LEF. At CAR the discrepancies are due to mismatch in the time of day the data is collected.

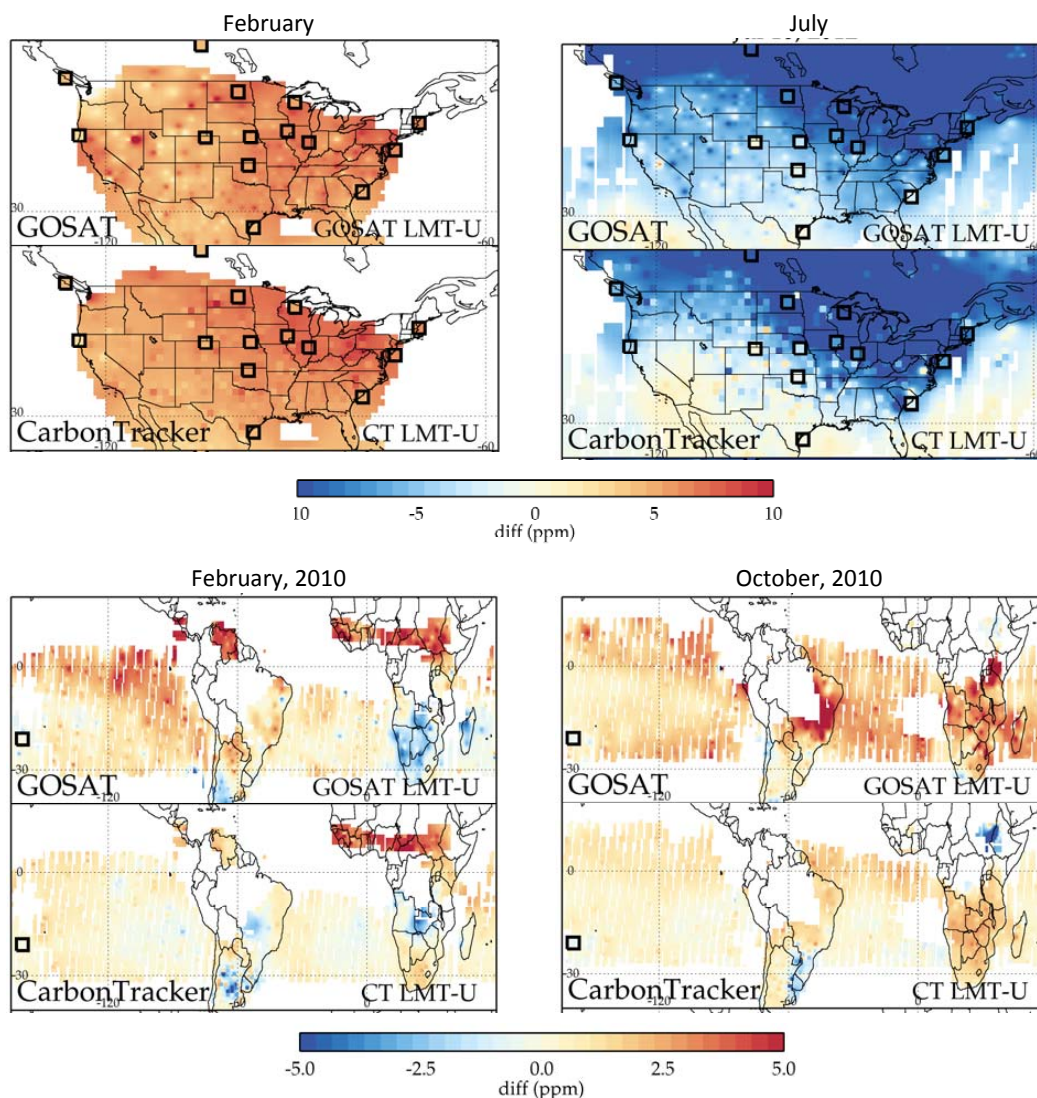


Figure 12. LMT – U differences. LMT – U diagnoses model vertical transport (Stephens, 2007) and transport of outflow (Deeter, 2013). Results shown for the U.S. (top) and South America/Africa (bottom) for two different months. GOSAT is shown on the top and CarbonTracker on the bottom. Aircraft LMT – U differences are shown in the squares. There is agreement in the U.S. where there is a lot of surface-based data to ingest into CarbonTracker, but disagreement in southern Africa during the growing season in February, the Amazon region in the biomass burning season in October, and in the outflow from Africa and South America in October.